FEASIBILITY STUDY OF A ROBOTIC PLASMA MEDICINE DEVICE USING NUMERICAL SIMULATION

A Thesis

by

WILL BRENDAN MCKINNEY

Submitted to the Office of Graduate and Professional Studies of
Texas A&M University
in partial fulfillment of the requirements for the degree of

MASTER OF SCIENCE

Chair of Committee,	Seok Chang Ryu
Committee Members,	Kentaro Hara
	Bruce Tai
Head of Department,	Andreas A. Polycarpou

August 2019

Major Subject: Mechanical Engineering

ABSTRACT

A concept design of a robotic plasma medicine device is presented, which can generate cold atmospheric plasma (CAP) inside of the human body and deliver CAP through a dynamically moving tip to treat exposed cancers. To explore the feasibility of the design concept, numerical models are developed using COMSOL v5.4, a commercially available finite element analysis modeling software. However, due to the limitations of the current state-of-the-art simulation technologies, an individualized physics approach to this problem is necessary. Using three decoupled physics models, the stability of gas flow, the electrical insulation required for safe in vivo use, and the effects of various design and operating parameters on the plasma are investigated. Design and operating parameters studied in this research include tip velocity, tip angle, applied voltage, and electrode spacing. The effect a dynamic tip has on the radial velocity profile exiting the device was revealed by the neutral gas flow study. Thus, a decreased angular tip velocity would be required to reduce these potential effects when treating larger areas. The results from the electrostatics study ensured that there was no electric field outside of the device, and the ground shield would prevent any potential breakdown from occurring externally. Additionally, the region of the insulation containing electric field values greater than the insulation's dielectric strength was significantly localized. The plasma operation study demonstrated the effects of varying the electrode spacing and applied voltage on the discharge characteristics including electron density, electron temperature, discharge current, and plasma power. The afterglow chemistry model allowed a connection to made in terms of how the plasma discharge characteristics produced in the variance of applied voltage and electrode spacing effect a device's potential ability to treat cancer through the generation of reactive oxygen species (ROS) including O, $O_2(^1D)$, O_3, OH, HO_2, H_2O_2, and O_2^-. Both 5 mm and 10 mm electrode spacings demonstrated the ability to produce relatively high concentrations of ROS across a voltage range of 5 kV to 10 kV.

ACKNOWLEDGMENTS

I would like to express my sincere gratitude to my advisor, Dr. Ryu, for his guidance and providing me with an opportunity to work on this project. I would like to thank Dr. Hara for the time, guidance, and help he provided me in performing plasma simulations. I would also like to express my appreciation to Dr. Tai for his review, input, and support. Finally, I wish to thank my parents for their continuous support in my education.

CONTRIBUTORS AND FUNDING SOURCES

Contributors

This work was supported by a thesis committee consisting of Dr. Ryu and Dr. Tai of the Department of Mechanical Engineering and Dr. Hara of the Department of Aerospace Engineering. All work conducted for the thesis was completed by the student independently.

Funding Sources

Graduate study was not supported by any funding sources.

TABLE OF CONTENTS

Page

LIST OF FIGURES

FIGURE Page

LIST OF TABLES

TABLE Page

1. INTRODUCTION

Plasma, known as the fourth state of matter, is composed of electrons, ions, and neutrals. Plasma is created when a sufficient amount of energy is applied to a neutral gas. Consequently, the gas is partly or fully ionized. In a laboratory setting, the energy applied to the neutral gas is typically applied via an electric field. Plasma can be classified into two categories based on the temperature of its constituents: Thermal and Non-Thermal. Thermal plasmas are assumed to be in a state of local thermodynamic equilibrium (LTE). This means that the temperature of the electrons, ions, and neutrals are equal. On the contrary, non-thermal plasmas are not in thermal equilibrium. The temperatures of the heavier particles, ions and neutrals, are much lower than the temperature of the electrons. These plasmas are weakly ionized allowing the gas chemistry to be preserved without increasing the gas temperature. Non-equilibrium plasma, also known as low-temperature plasma (LTP) or cold plasma, has a gas temperature that is close to room temperature. This quality makes LTP sources appealing for a variety of applications. Low-temperature plasma is modeled in this thesis and is the topic of focus for this research.

1.1 Plasma Medicine

Plasma medicine is the multidisciplinary field, at the intersection of physics, engineering, biology, and medicine, that involves the biomedical applications of low-temperature plasma [3]. Some of these applications include sterilization, dental care, wound healing, and most notably cancer treatment. There have been numerous studies that have presented the anti-cancer effects of LTP including the ability to selectively kill cancer cells in vitro and reduce tumor size in vivo [4]. Table 1.1 highlights publications that have demonstrated the effectiveness of LTP treatment on several cancer types both in vitro and in vivo.

Most investigations have reported a dose-dependent effectiveness of plasma treatment. More specifically, the mode of cell death is dose dependent. Low doses of plasma result in apoptosis while high doses lead to necrosis [14, 15]. Apoptosis, the process of programmed cell death, is the

Table 1.1: Plasma medicine: operating parameters and various cancer treatment results.

Cell type/tumor	**Method**	**Plasma device**	**Flow rate**	**Freq.**	**Voltage**	**Exposure time**	**Op. dist.**	**Result**
Human colon carcinoma cells, mouse melanoma cells, normal macrophages	In vitro	Plasma jet	1-5 LPM (He)	100 pps	20 kV	60, 120 s	10 mm	Selective cell death of tumor cells [5]
Human glioblastoma cells	In vivo	FE-DBD		100 Hz	17 kV	2 min x 3 times/day	2 mm	Reduction of tumor volume after 5 days of treatment [6]
Human melanoma cells, human primary keratinocytes	In vitro	Plasma jet		113 kHz square wave	2.5 kV	10 s	2 mm	Selective cell death of melanoma cells [7]
Mouse melamona cells, human lung cancer cells, human bladder cancer cells	In vitro In vivo	Plasma jet	10-20 LPM (He)	30 kHz	3-5 kV	0, 30, 60, 120 s, 2-5 min	10 mm	Selective cell death, apoptosis, decreased tumor volume, overall survival, 5 mm tumor ablated by 2 min treatment [8]
Human pancreatic cancer	In vitro In vivo	Plasma jet	480 SCCM (He)	2kHz	13 kV	10 min	2 mm	Significant reduction of tumor size by combination of CAP + Gemcitabine in vivo [9]
Human bladder cancer cells	In vitro	Plasma jet	5 LPM (He)	5kHz, pulse width = 800 ns	7 kV	2, 3.5, 5 min	20 mm	Apoptosis, viability of cells reduced with increased treatment time [10]
Mouse breast cancer cells	In vitro In vivo	Plasma jet	0.5 LPM (He)	6 kHz	4 kV	3 min	10 mm	Apoptosis, suppressed tumor growth [11]
Human bladder cancer cells	In vitro	Plasma jet	5 LPM (He)	5kHz, pulse width = 800 ns	7 kV	2, 3, 4, 5 min	22 mm	Significant reduction of cell viability for 2, 3 min of treatment time [12]
Human glioblastoma cells, human breast cancer cells	In vitro	Plasma jet	4-5 LPM (He)	13 kHz	3-6 kV	30, 60, 90, 180 s	20 mm	Apoptosis, reduction in cancer cell viability with increased treatment time, 3.16 kV discharge voltage optimal in reduction of cell viability [13]

Abbreviations: Freq. – Frequency, Op. dist. – Operating distance, FE-DBD – Floating electrode dielectric barrier discharge, LPM – liters per minute, SCCM – standard cubic centimeters per minute, pps – pulses per second.

favorable mode of cell death as it results in no harmful effects. It is typically apart of various vital processes including "normal cell turnover, proper development and functioning of the immune system, hormone-dependent atrophy, embryonic development and chemical-induced cell death" [16]. Alternately, the opposite of apoptotic cell death is necrosis, and it is considered a toxic process that results in cell swelling, disruption of the cell membrane, and inflammation.

While the mechanism behind the selective eradication of cancer cells is not entirely understood, the abundance of reactive oxygen and nitrogen species (RONS) generated by CAP are believed to play a significant role [17, 18]. As shown in Figure 1.1, a plasma device is capable of directly producing reactive species in the afterglow region when the core plasma is introduced with air. Subsequently, the produced species are delivered to the cancer cite. According to [17] and [18], the reactive oxygen species (ROS), such as atomic oxygen (O), singlet-delta oxygen ($^1O_2$), ozone (O_3), hydroxyl (OH), hydroperoxyl (HO_2), and hydrogen peroxide (H_2O_2), potentially promote a "killing effect" while the reactive nitrogen species (RNS), such as nitrite oxide (NO), may produce a "healing" effect [18]. The exact role that each of these species play in treating cancer is unknown.

The precise control of the plasma dose and the factors influencing it are considered vital for several reasons. These reasons include the selective killing of cancer cells without harming normal cells, nontoxic cell death, and keeping the treated tissue at a tolerable temperature. In general, the applied plasma dose can be defined as a function of the gas flow rate, plasma power, and exposure time. However, the plasma power is influenced by countless factors such as the plasma device design and size, applied voltage, and operating distance. The operating distance is defined as the distance from the tip of the device to the treatment surface. As shown in Table 1.1, the operating conditions used to treat cancer varies from device to device. This can be contributed to many parameters including the device size, dielectric material, electrode size and spacing, gas flow rate, operating distance, and cancer type. Thus, it is difficult to gauge the plasma power, and consequently the applied dose, without evaluating the effect of specific device design and operating parameters. Furthermore, an in-depth understanding of individual device operating and design parameters is required in order to tailor the plasma power for each type of cancer.

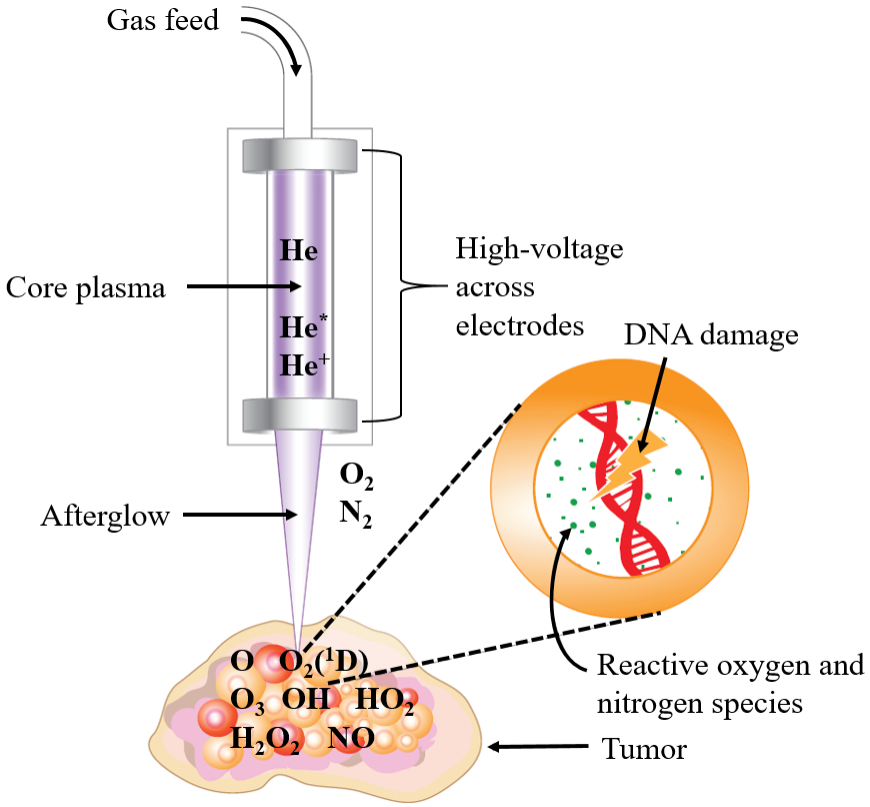

Figure 1.1: Plasma device showing production of reactive species in the application of cancer treatment. Adapted from [1].

1.2 Modeling of Plasma

There have been many studies that have modeled non-thermal atmospheric plasma jets [19, 20, 21] as well as evaluated the effect of design and operating parameters for specific devices on the plasma [22, 23, 24]. While there may be trends in the effects that such parameters have, the exact result varies from device to device depending on the device size, electrode configuration, dielectric material, and operating conditions. Consequently, there is a need to gain a thorough understanding of the robotic plasma device under investigation for the application of precise treatment of cancer. Additionally, no studies have addressed the flow of plasma through a moving tip. Recently, [25] and [26] created feedback control models that demonstrated the ability to adjust plasma operating conditions in real time in response to variations in the plasma and to the effectiveness of killing cancer cells. While the real time control of a device in cancer treatment is the ultimate goal, an

in-depth understanding of the robotic device in this research, specifically its design, must first be obtained.

COMSOL Multiphysics is simulation software and finite element analysis solver for various physics and engineering problems, including coupled phenomena [27]. It permits the use of conventional physics-based user interfaces as well as the input of coupled systems of partial differential equations (PDEs). COMSOL version 5.4 was used for the purpose of this research.

The laws of physics for space- and time- dependent problems can typically be expressed as PDEs. However, for a majority of engineering problems these equations are unable to be solved analytically due to complexity in geometry and physics. An approximation of these equations can be formulated into numerical model equations based on discretizations. Numerical methods can then be utilized to solve an estimate of the PDEs through numerical model equations. Thus, the generated solution is an approximation of the actual solution to the PDEs. The finite element method (FEM) is used to calculate such approximations [28]. With the finite element method, the domain under investigation is discretized by dividing the domain into smaller subdomains called elements. The weighted residual method is then used to approximate a solution within each element. FEM is the default method used by COMSOL for performing simulations and was used for this research.

A simulation in COMSOL Multiphysics is performed by following a procedural flow as presented in Figure 1.2. The procedure can be divided into three main steps of pre-processing, solve, and post-processing. The pre-processing step involves building the model and can be split into sub-steps. The first sub-step consists of creating the computational geometry and assigning material properties to specific domains. Next, the physical settings of the problem are produced by assigning the underlying physics, mathematical equations, and finite element formulation to the model [29]. The necessary boundary conditions, initial conditions, and loadings are then defined for the domain under investigation. After the computational domain is discretized into finite elements by generating a mesh, the matrix equations are formed that govern the model. Once, pre-processing is finished, the set of algebraic equations are solved to find the physics-related nodal solutions of

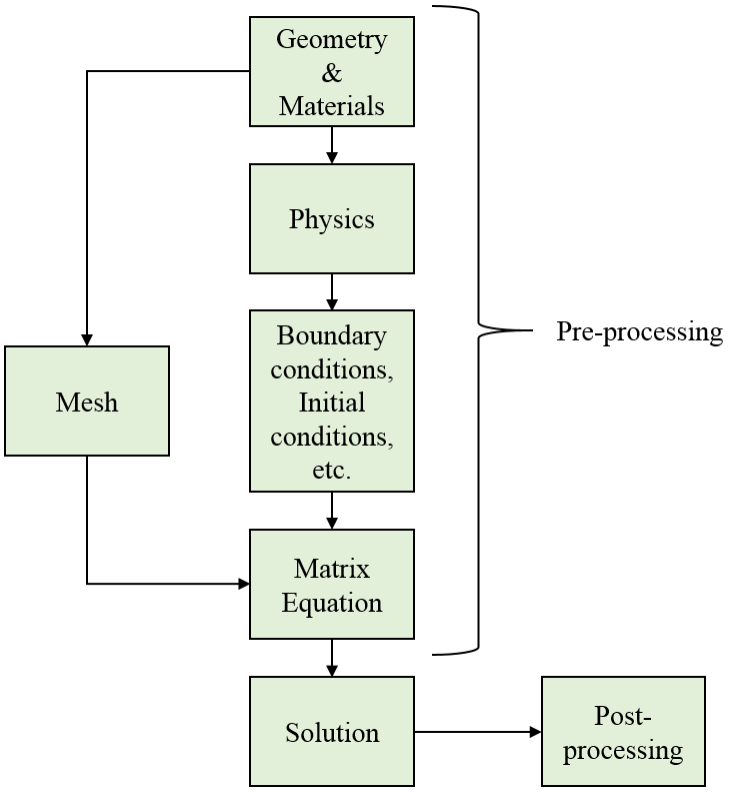

Figure 1.2: Basic steps to perform a simulation in COMSOL Multiphysics.

the model. Lastly, post-processing allows for the computed solution to be analyzed by creation of plots and exportation of data.

COMSOL is used in this thesis to study the physics involved in the operation of a robotic plasma medicine device. The studies performed used the following models/physics:

1. Laminar flow (spf);
2. Electrostatics (es);
3. Plasma (plas).

An overview of the physics and the equations used by the solver are discussed in detail in the Theory section of each study.

1.3 Concept Design

The robotic plasma device under investigation in this work is shown in Figure 1.3. It has been designed for in vivo treatment of cancer. The device is equipped with a 1 degree of freedom (DOF) distal tip that can be actuated with tendons via servomotors. The steerable tip allows for device maneuverability in vivo, treatment of various sized tumors, and favorable tip orientation during operation. The plasma jet configuration consists of two copper ring electrodes, one powered and one grounded, around the outside of a borosilicate glass tube that serves as a dielectric as well as the gas flow channel. The proximal and distal part of the device is connected by a hinge joint that enables the tip actuation. The proximal glass tube and distal glass tube is joined by a flexible silicone tube. Additionally, electrically insulating epoxy surrounds the plasma components with a grounded metallic shield enclosing the insulation. Nonetheless, the feasibility of the device needs to be studied in terms of safety and efficacy. Numerical simulations provide an economical manner to do so.

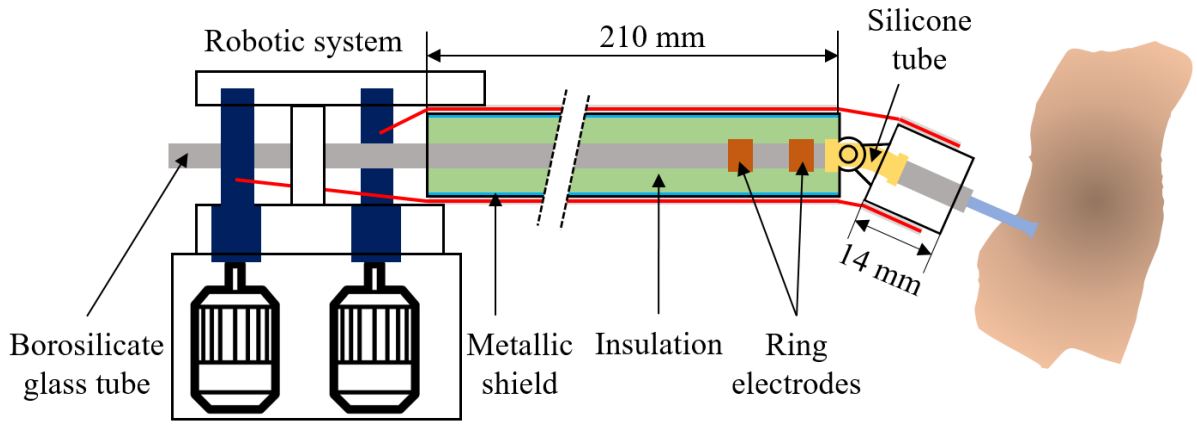

Figure 1.3: Schematic of robotic plasma device treating tumor. The device components are color coded as follows: insulation (green), dielectric tube (gray), flexible silicone tube (yellow), electrodes (brown), metallic shield (blue), tendons (red). Adapted from [2] © 2019 IEEE.

The plasma device studied in this research is similar to the plasma device used to treat bladder cancer cells in [10] and [12]. The electrode arrangement, consisting of a powered and grounded

ring electrode embedded in a dielectric tube, is similar to electrode configuration investigated in this study. Therefore, an acceptable applied voltage range for treating cancer was estimated to be 5 to 10 kV for this work.

1.4 Objectives

This thesis explores the practicality of a robotic plasma medicine device designed to treat cancer in vivo. More specifically, it seeks to prove the feasibility of generating stable, controlled plasma flow through a dynamically moving tip, which is vital for selective treatment of cancer. To do so, numerical simulations will be performed with COMSOL, a FEM software that is capable of solving multiphysics problems and handling the instabilities present in a plasma simulation. Due to limitations in the current state-of-the-art simulation technologies, an individualized physics approach is necessary to simulate the flow of plasma through a moving tip. Thus, the gas flow is studied independently from the plasma. The effect of tip angle and angular tip velocity is investigated on the gas flow. Additionally, the effect of design and operating parameters, including applied voltage and electrode spacing, on the plasma is studied to acquire the ideal parameters for in vivo use. The device safety is evaluated by studying the electrical insulation of the device, which is important for safe use in vivo. This is achieved with an electrostatics simulation in COMSOL. The results obtained from this work will allow a better understanding of design and operating parameters of the plasma device required for safe operation and controlled treatment. The following objectives and metrics were defined to justify this research.

1. Investigate the effect of dynamic tip motion on gas flow, i.e. the potential stability of the plasma plume
    (a) Identify gas flow regime and compressibility of helium in flow
    (b) Perform gas flow simulations with static and dynamic tip
        i. Quantify effect by examination of radial velocity profile at exit of tube
        ii. Compare results of static and dynamic tip at various tip angles

2. Evaluate electrical safety of the proposed device

    (a) Perform electrostatics simulations for three different insulation thicknesses at two applied voltages

        i. Evaluate distribution of electric field across insulation

3. Investigate the effect of design and operating parameters on the properties of plasma plume generated

    (a) Perform plasma simulations for three different electrode spacings at three applied voltages

        i. Identify effect of varied electrode spacing and applied voltage on electron density, electron temperature, discharge current, plasma power, and ROS densities

        ii. Determine ideal electrode spacing for operating within predefined voltage range for treating cancer

In addition, the limitations in the current simulation technology for studying a robotic plasma device will be identified.

This thesis is organized as follows. Section II presents the neutral gas flow study. Section III presents the safety study including an electrostatics analysis. Section IV presents the plasma study and discusses the limitations of numerical plasma simulations. In each of these sections, the study purpose, theory behind the physics, model setup, and simulation results are discussed in detail. Finally, the conclusions and recommendations for future work are presented in Section V.

2. NEUTRAL GAS FLOW STUDY

2.1 Model Overview

2.1.1 Purpose

Stable flow of plasma is important in a plasma medicine device. The flow and delivery is often considered to be governed by the gas flow as shown in studies by [30] and [31]. However, the effect of the dynamic tip on the gas flow is unknown and must be investigated. The purpose of the neutral gas flow study was to examine the effect of tip angular velocity and tip angle on the exit volumetric flow rate of the gas. There was some concern as to how much the angular tip velocity and tip angle may have an effect on the average velocity or flow rate exiting the device which would have an effect on an administered dosage rate. In order to fully investigate the effect of a dynamic tip on the gas flow, both static and dynamic tip simulations were performed. First, simulations were performed with a static tip fixed at angles of -30^o, -15^o, 0^o, 15^o, and 30^o. Next, simulations were performed with a dynamic tip defined to oscillate from 0^o to 30^o, 30^o to -30^o, and -30^o to 0^o over a prescribed time interval. Lastly, the radial velocity profiles at the tube exit were compared for the static and dynamic tip cases. Prior to performing the study, the characteristics of the gas flow were evaluated as discussed in the Theory section. Helium gas is more easily ignited at atmospheric pressure in comparison to other gases such as argon and neon, commonly used in medical applications [11, 32], and cost effective. For these reasons, it was chosen as the working gas in this study and throughout this thesis. Additionally, a flow rate of 3 LPM (liters per minute) was selected for this simulation because it falls within the operating range of previous cancer treatment studies as shown in Table 1.1.

2.1.2 Theory

The characteristics of helium gas flow were investigated prior to running simulations in order to determine the gas flow regime as well as if the gas should be considered compressible or incompressible. The Reynolds number, a dimensionless quantity defined as the ratio of inertial forces

to viscous forces, was calculated to characterize the flow regime. The gas flow in this study was operating in the laminar flow regime as characterized by a Reynolds number of 130 using Eq. 2.1, where ρ is the density of the gas (ρ = 1.625 kg/m^3, u is the average velocity of the gas, D is the inner tube diameter, and μ is the dynamic viscosity of the gas (1.99 x 10 $^{-5}$ Pa s). To assess if the gas could be considered incompressible, the Mach number, the ratio of speed of flow, u, to speed of sound in the gas, c, was computed using Eq. 2.2.The speed of sound in helium was calculated using Eq. 2.3 where k is the ratio of specific heats (k= 1.67), R is the gas constant (R=2077 J/(kg·K)), and T is the absolute temperature of the gas (T=300 K). The gas was considered incompressible because the Mach number was well below 0.3, the threshold for considering a gas incompressible.

$$Re = \rho_d \mathrm{u} D/\mu \tag{2.1}$$

$$M = \mathrm{u}/c \tag{2.2}$$

$$c = \sqrt{kRT} \tag{2.3}$$

The gas flow is governed by the mass continuity equation (Eq. 2.4) and the Navier-Stokes momentum conservation equations (Eq. 2.5), where ρ_d is the density, **u** is the velocity field, p is the pressure, μ is the dynamic viscosity, and **F** is the body force. Eq. 2.4 and Eq. 2.5 were solved by a time dependent solver in COMSOL (McKinney, Feasibility Study of In Vivo Robotic Plasma Medicine Devices, International Symposium on Medical Robotics)

$$\nabla \cdot (\rho_d \mathbf{u}) = 0 \tag{2.4}$$

$$\rho_d(\frac{\partial \mathbf{u}}{\partial t} + \mathbf{u} \cdot \nabla \mathbf{u}) = -\nabla p + \nabla \cdot (\mu(\nabla \mathbf{u} + (\nabla \mathbf{u})^T) + \mathbf{F} \tag{2.5}$$

2.1.3 Model Setup

A 2D steerable tube model was built in COMSOL Multiphysics. The computational domain geometry, shown in Figure 2.1, consisted of two glass tubes (D_{in} = 4 mm, D_{out} = 6.35 mm) connected by a silicon tube (D_{in} = 4 mm, D_{out} = 6.35 mm) with an 'atmospheric domain' at

the exit of the tube. A mesh consisting of 129,024 free triangular elements was generated with refinement at the inlet and exit of the tube to accurately monitor the flow rate and velocity. Helium gas was defined as the neutral gas filling the fluid domain. A constant velocity of 3.979 m/s was defined at the inlet of the tube to comply with a flow rate of 3 LPM. A pressure outlet (P = 1 atm) was defined along the outer boundaries of the 'atmospheric domain' (McKinney, Feasibility Study of In Vivo Robotic Plasma Medicine Devices, International Symposium on Medical Robotics)

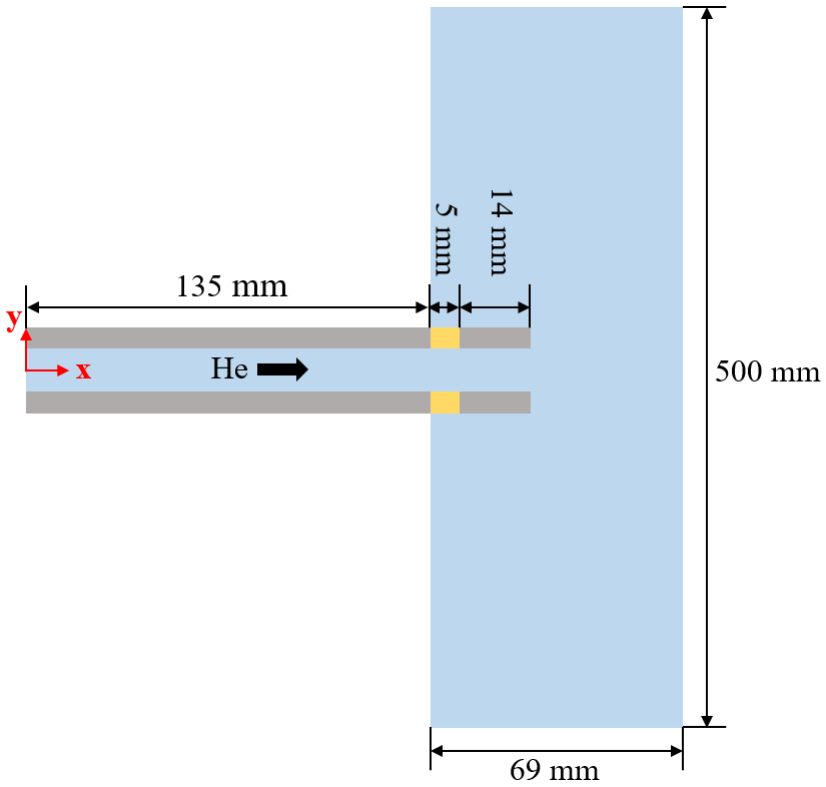

Figure 2.1: Computational domain (not to scale) used for gas flow simulation.

An oscillating motion, causing the tip (5 mm silicone tube in connection with 14 mm glass tube) to bend from 0° to 30°, down to -30°, and back to 0° over a prescribed interval of time was defined for the wall domains of the tip. To do so, equations for the bending of a cantilever beam with an intermediate applied load were used. The assumptions used in the derivation of these

equations include pure bending, linear elastic material, small deflections, and negligible shear force contribution to the deflection. Pure bending presumes that the tip is straight prior to loading, constant cross-sectional area, the tip has a longitudinal plane of symmetry in which the bending moment lies, the bending moment does not vary with length, and the tip material is homogeneous and isotropic [33]. The deflection of the neutral axis of the tip in the y-direction was defined by Eq. 2.6 for the silicon tube (δ_1) and Eq. 2.7 for the distal glass tube (δ_2), where F is the applied force required to displace the tip 30°, X is the x-distance along the tube length, E is the modulus of elasticity of silicon (E = 25.5 MPa), I is the moment of inertia of the tube (I = 67.245 mm^4), and L_1 is the length of the silicon tube (L_1 = 5 mm). The force required to displace the tip 30° was defined using the expression $F = -79.2$[N] $sin(\omega t)$ to generate an oscillatory bending motion from 0° to 30°, down to -30°, and back to 0° over time, t, where ω = $2\pi f$ and f = 1 / T. For the dynamic tip study, the time period to complete a single oscillatory cycle, T, was defined to be 20 seconds for one simulation, which corresponded to an average angular tip velocity of 6°/s, and 8 seconds for another simulation, which corresponded to an average angular tip velocity of 15°/s. These two angular velocities were chosen to represent a possible slow and fast tip operation velocity.

$$\delta_1 = \frac{FX^2}{6EI}(X - 3L_1) \tag{2.6}$$

$$\delta_2 = \frac{FL_1^2}{6EI}(L_1 - 3X) \tag{2.7}$$

The angle along the length of the tip, with respect to the horizontal, was defined by Eq. 2.8 for the silicon tube (θ_1) and Eq. 2.9 for the distal glass tube (θ_2).

$$\theta_1 = tan^{-1}(\frac{F}{2EI}(X^2 - 2L_1X)) \tag{2.8}$$

$$\theta_2 = tan^{-1}(-\frac{FL_1^2}{2EI}) \tag{2.9}$$

Since the above equations were derived for the neutral axis of the tip, they were altered to define the deflection of the inside surface of the tip walls. A prescribed displacement was defined in COMSOL for the top and bottom wall domains of the tip. Eqs. 2.10 and 2.11 were used to specify the displacement in the x- and y- direction of the top wall of the silicon tube as denoted by X_{top_1} and Y_{top_1}, where D_{in} is the inner diameter of the tube (D_{in} = 4 mm).

$$X_{top_1} = -\frac{D_{in}}{2} sin(\theta_1) \tag{2.10}$$

$$Y_{top_1} = \delta_1 - \frac{D_{in}}{2} + \frac{D_{in}}{2} cos(\theta_1) \tag{2.11}$$

Eqs. 2.12 and 2.13 were used to specify the displacement in the x- and y- direction of the bottom wall of the silicon tube as denoted by X_{bottom_1} and Y_{bottom_1}.

$$X_{bottom_1} = \frac{D_{in}}{2} sin(\theta_1) \tag{2.12}$$

$$Y_{bottom_1} = \delta_1 + \frac{D_{in}}{2} - \frac{D_{in}}{2} cos(\theta_1) \tag{2.13}$$

Eqs. 2.14 and 2.15 were used to specify the displacement in the x- and y- direction of the top wall of the distal glass tube as denoted by X_{top_2} and Y_{top_2}.

$$X_{top_2} = -\frac{D_{in}}{2} sin(\theta_2) \tag{2.14}$$

$$Y_{top_2} = \delta_2 - \frac{D_{in}}{2} + \frac{D_{in}}{2} cos(\theta_2) \tag{2.15}$$

Eqs. 2.16 and 2.17 were used to specify the displacement in the x- and y- direction of the bottom wall of the distal glass tube as denoted by X_{bottom_2} and Y_{bottom_2}.

$$X_{bottom_2} = \frac{D_{in}}{2} sin(\theta_2) \tag{2.16}$$

$$Y_{bottom_2} = \delta_2 + \frac{D_{in}}{2} - \frac{D_{in}}{2} cos(\theta_2) \tag{2.17}$$

These same equations were used to determine the tip geometry for the static case with fixed tip angles. The force required to displace the tip, F, $\pm$ 15° and $\pm$ 30° was defined to be $\pm$36.8 N and $\pm$ 79.2 N, respectively.

The static and dynamic tip simulations were run with a time dependent solver in COMSOL. The static case was run for a duration of 5 s with time steps of 0.1 s. The results were evaluated at a time of 5 s. The dynamic case, for an angular tip velocity of 6°/s, was run for a duration of 20 s with time steps of 0.1 s. The results were evaluated at times of 1.536 s, 5 s, 10 s, 11.536 s, and 15 s which corresponded to tip angles of 15°, 30°, 0°, -15°/s, and -30°. The dynamic case, for an angular tip velocity of 15°/s, was run for a duration of 8 s with time steps of 0.04 s. The results were evaluated at times of 0.6144 s, 2 s, 4 s, 4.6144 s, and 6 s which corresponded to tip angles of 15°, 30°, 0°, -15°/s, and -30°. The radial velocity profiles at the exit of the tip were generated according to the radial coordinate system defined in Figure 2.2.

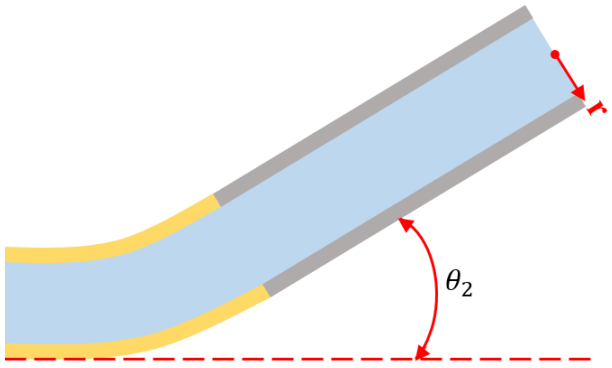

Figure 2.2: Bent tip schematic defining radial coordinate system at exit of tip.

2.2 Results and Discussion

The average velocity and consequently the flow rate remained constant from the inlet to the exit of the tube because helium was considered incompressible based on the Mach number of the flow. Therefore, the prescribed flow rate was unchanged regardless of tip angle or angular tip velocity. The velocity profile at the exit of the tube was evaluated for both a static tip and dynamic tip at tip angles of -30°, -15°, 0°, 15° and 30°. For the static case, the velocity profile was essentially unaffected by the tip angle as presented in Figure 2.3. The velocity magnitude peak at the exit of the tube remained constant at 5.92 m/s for all tip angles. However, the peak velocity was slightly shifted radially based on the tip angle, with the greatest shifts of -0.04 mm and 0.04 mm being at -30° and 30°, respectively. These shifts were considered negligible. For the dynamic case, which

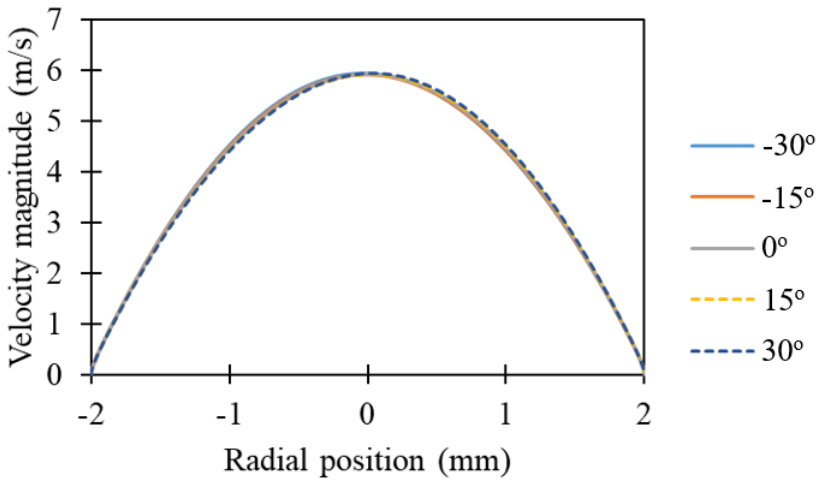

Figure 2.3: Radial velocity profile at exit of tube at various tip angles for static tip.

was run at an angular tip velocity of 6°/s, the velocity profile at the exit of the tube was altered with respect to the tip angle as displayed in Figure 2.4. The peak of the velocity was shifted radially from the center of the tube as angle was increased, but the maximum velocity remained constant at 5.92 m/s. The radial shift in the maximum velocity at tip angles of -15° and 15° was -0.35 mm and 0.29 mm, respectively. This was approximately half of the radial shift exhibited at -30° and 30°,

which was determined to -0.62 mm and 0.57 mm. At a tip angle of 0°, when the tip was moving from 30° to -30°, the peak velocity was shifted a radial distance of 0.03 mm. For the dynamic case,

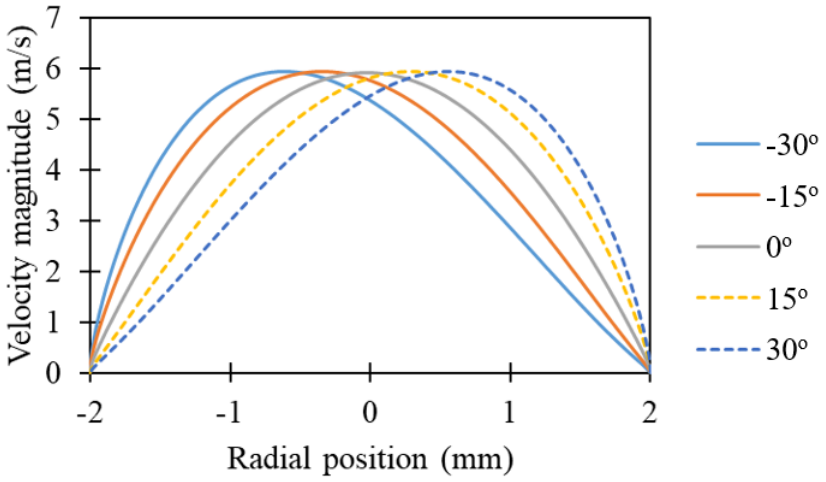

Figure 2.4: Radial velocity profile at exit of tube at various tip angles for dynamic tip moving at 6°/s.

which was run at an angular tip velocity of 15°/s, the velocity profile at the exit of the tube was altered with respect to the tip angle as displayed in Figure 2.5. The maximum velocity remained constant at 5.92 m/s for all tip angles. The radial shift in the maximum velocity at tip angles of -15° and 15° was -0.38 mm and 0.26 mm. The radial shift at -30° and 30° was -0.66 mm and 0.54 mm. At a tip angle of 0°, the peak velocity was shifted a radial distance of 0.06 mm.

When comparing the radial velocity profiles between the static and dynamic tip, the peak velocity shift was magnified with the moving tip. The core shift was present in the static case, but was insignificant with a maximum radial shift of 0.04 mm at the greatest tip angle. However, this shift was magnified by approximately 15 times in the dynamic cases. There were no significant differences between the exit velocity profiles for angular tip velocities of 6°/s and 15°/s. The faster angular tip velocity yielded a slight increase in the velocity peak shift for negative angles and a slight decrease in the velocity peak shift for positive angles. Additionally, at a tip angle of 0°, the faster angular tip velocity caused the maximum velocity to shift a radial distance twice that

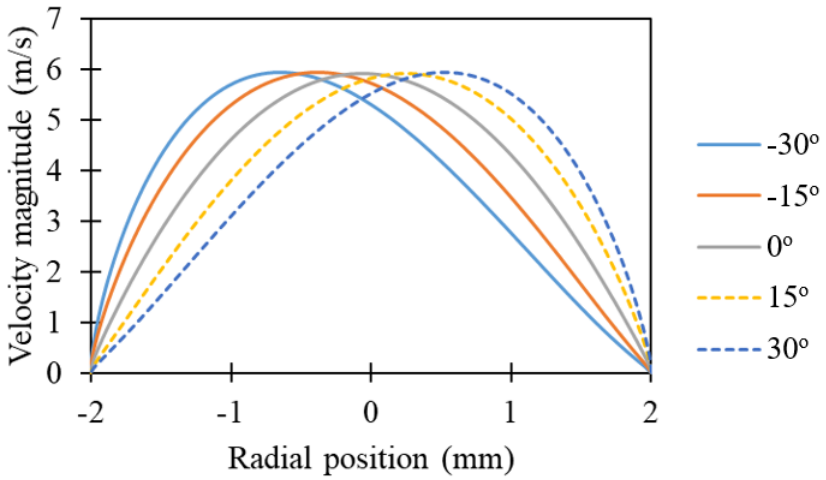

Figure 2.5: Radial velocity profile at exit of tube at various tip angles for dynamic tip moving at 15°/s.

of the slower angular tip velocity. Theoretically, the velocity peak should have shifted the same amount for positive and negative angles. A possible reason for this error in the dynamic tip simulations is the deforming of the mesh around the moving geometry which requires the mesh elements to deform and resize during the simulation. Inconsistent deforming of the mesh for positive and negative angles may have led to such differences.

The shift in the velocity profile through an angled tip can be contributed to the radial pressure gradient developed by the centripetal force acting on the gas. The pressure gradient caused the gas at the center of the tube, where the flow velocity is highest, to shift towards the outer wall. This phenomenon was seen in the gas flow simulations. The increased radial shift in the velocity core from the static case to the dynamic cases can be contributed to the fact that the static case was evaluated when the gas flow was at a steady state. Hence, the flow had sufficient time and tube length to recover from the bend. Since the tip, after the bent portion, is 4.5 tube diameters long, this was sufficient length for the flow to develop into practically fully-developed flow at the exit as evident by minimal changes in the radial velocity profile. However, with the dynamic cases the flow did not transform to fully-developed flow post bend because the tip was moving. Thus, the flow did not have sufficient time to reach fully developed flow because the angle was constantly

changing and shifting the velocity core.

The dynamic effect on the gas flow is considered significant and may be a reason for concern for treating cancer. Possible concerns for the radial shift in the velocity core include increased loss of charged species, which are known for helping treat cancer, to the tube walls, and uneven delivery of plasma products to the tumor surface. A slower angular tip velocity may help minimize the shift in the core of the velocity profile if the tip is required to move for treating larger areas.

3. SAFETY STUDY: ELECTROSTATICS

3.1 Model Overview

3.1.1 Purpose

Safe device operation is required for in vivo use. Any electrical failure is unacceptable and could be catastrophic. The insulation necessary for safe operation of the plasma device is unknown and must be investigated. The purpose of the safety study was to investigate the electrical insulation of the plasma device. More specifically, the focus was to examine the electric field inside the device. Due to the application of high voltages required to generate plasma, there was some concern for potential breakdown of the insulation surrounding the electrodes during operation. In order to thoroughly investigate the electric field inside the device, simulations were run for different insulation thicknesses at various applied voltages. Simulations were performed for insulation thicknesses of 3.5 mm, 4.5 mm, and 5.5 mm at two different applied voltage amplitudes of 6 kV and 12 kV, which are representative of a possible operating voltage and a voltage above a possible operating voltage.

3.1.2 Theory

The electric field, **E**, is governed by Poisson's equation (Eq. 3.1) in the gas region and Laplace's equation (Eq. 3.2) in the dielectric material, where ε_o is the permittivity of free space, ε_r is the relative permittivity, ρ_c is the space charge density, and V is the applied potential. The system of Eqs. 3.1-3.3 were solved by a time dependent solver in COMSOL (McKinney, Feasibility Study of In Vivo Robotic Plasma Medicine Devices, International Symposium on Medical Robotics)

$$-\nabla \cdot \varepsilon_o \varepsilon_r \nabla V = \rho_c \tag{3.1}$$

$$-\nabla^2 V = 0 \tag{3.2}$$

$$\mathbf{E} = -\nabla V \tag{3.3}$$

3.1.3 Model Setup

The co-axial plasma jet device studied in this work was modeled using a 2D axisymmetric model in COMSOL Multiphysics. The computational domain geometry, shown in Figure 3.1, consists of a borosilicate glass tube, two copper ring electrodes, insulation of thickness t_{ins}, and aluminum shielding. The dielectric tube has an inner and outer diameter of 4 mm and 6.35 mm. The electrodes are 5 mm long, 0.09 mm thick, and separated by an axial distance of 15 mm. The shielding has a thickness of 0.07 mm. Helium gas was extended 2 mm around the exterior of the material domains to represent the working gas used in plasma generation as well as provide insight to potential breakdown outside the device. A mesh consisting of 546,630, 558,762, and 570,034

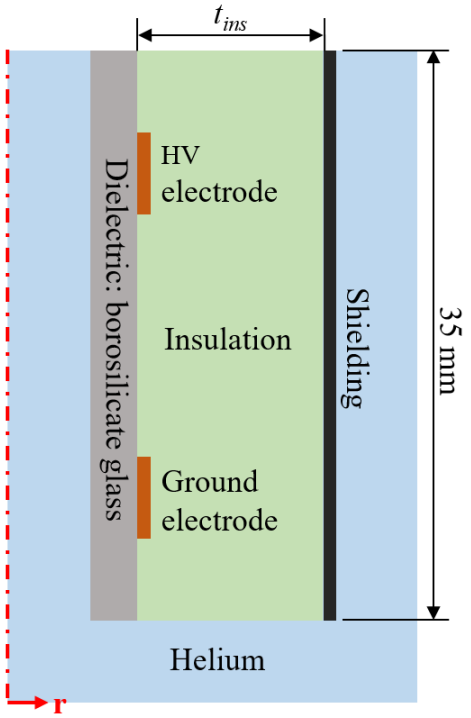

Figure 3.1: Computational domain (not to scale) used for electrostatic simulation; due to axisymmetric (r, z) nature of problem, only half of domain is shown. Adapted from [2] © 2019 IEEE.

free triangular elements, with refinement around the edges of the electrodes, was generated over

the entirety of the computational domain for insulation thicknesses of 3.5 mm, 4.5 mm, and 5.5 mm, respectively.

A sinusoidal voltage of the form shown in Eq. 3.4 was defined at the boundaries of the high voltage electrode, where V_o is the voltage amplitude, ω is the angular frequency equal to $2\pi f$. The frequency, f, was set to 20 kHz. The voltage amplitude was set to 6 kV or 12 kV. The boundaries of the ground electrode and shield were defined as grounded having a voltage represented by Eq. 3.5.

$$V = V_o sin(\omega t) \tag{3.4}$$

$$V = 0 \tag{3.5}$$

The relative permittivity of the two dielectric materials, borosilicate glass and the insulation (potting epoxy), were specified to be 4.6 and 2.883 based on the manufacturer's data sheets [34, 35] (McKinney, Feasibility Study of In Vivo Robotic Plasma Medicine Devices, International Symposium on Medical Robotics) © 2019 IEEE. Copper was assigned as the material for the electrodes and aluminum was assigned as the material for the shield, but their domains were excluded in the analysis because the potential is constant across a conductor.

3.2 Results and Discussion

The radial profiles for the electric field through the device for varying insulation thicknesses are shown in Figure 3.2(a) and Figure 3.2(b). These profiles were generated at a time, t, equal to 12.5 μs when the voltage was at a peak and from an axial location even with the center of the high voltage electrode. The electric field was highest right outside the high voltage electrode (radial distance = 0 mm). The discontinuity in the graph was at the ground shield where the electric field was reduced to 0 kV/mm (McKinney, Feasibility Study of In Vivo Robotic Plasma Medicine Devices, International Symposium on Medical Robotics) © 2019 IEEE.

The highest electric field values occurred at the edges of the high voltage electrode. A surface

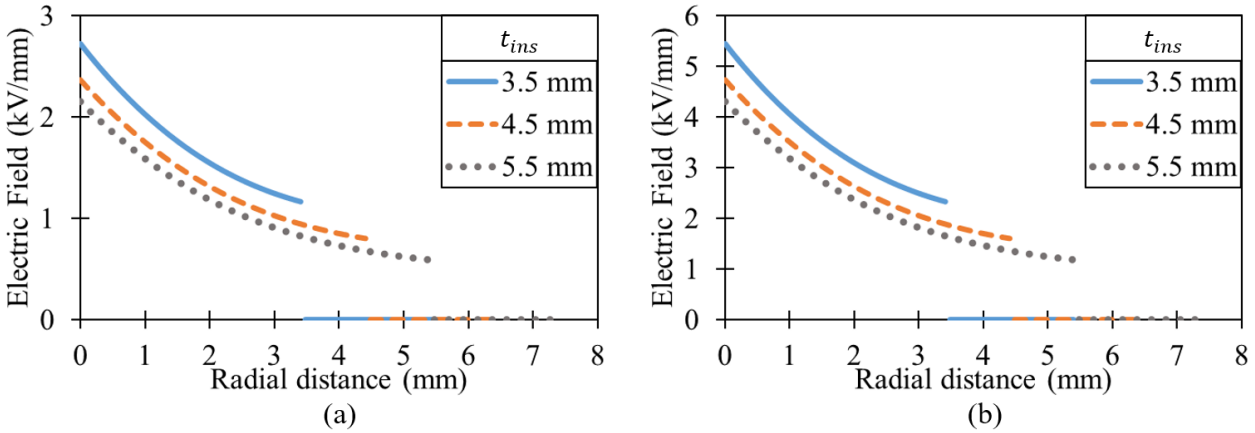

Figure 3.2: Radial profiles of electric field for an applied voltage of (a) 6 kV and (b) 12 kV. Adapted from [2] © 2019 IEEE.

contour of the electric field displays the distribution around the high voltage electrode in Figure 3.3(a) and Figure 3.3(b). The maximum electric field produced in the 3.5 mm insulation was 33.1 kV/mm for an applied voltage of 6 kV and 66.2 kV/mm for an applied voltage of 12 kV (McKinney, Feasibility Study of In Vivo Robotic Plasma Medicine Devices, International Symposium on Medical Robotics) © 2019 IEEE. These values decreased slightly with increasing insulation thickness. The maximum electric field was 30.1 kV/mm and 60.2 kV/mm for the 4.5 mm insulation and 28.2 kV/mm and 56.4 kV/mm for the 5.5 mm insulation.

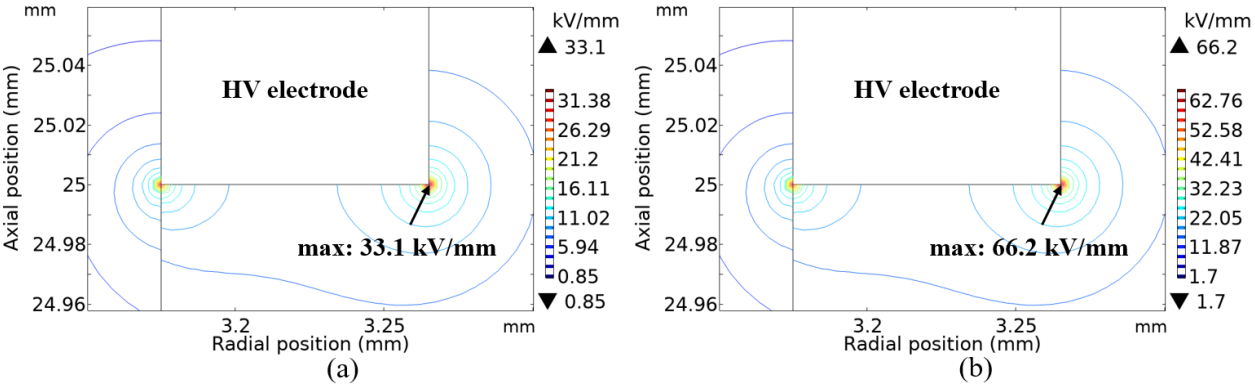

Figure 3.3: Electric field contour around high voltage electrode for an applied voltage of (a) 6 kV and (b) 12 kV. Adapted from [2] © 2019 IEEE.

The radial profiles for the electric field showed that the electric field decayed through the insulation and was reduced to zero at the grounded shield. This ensured that there was no electric field outside of the device and would prevent any potential breakdown from occurring externally. However, the radial electric field profiles did not show the maximum electric field inside the device. The maximum electric field occurred at the edges of the high voltage electrode. This provided insight as to where the most likely location of breakdown may occur based on the maximum electric field. The region with electric field values exceeding the insulation's dielectric strength of 15.9 kV/mm was localized. This region was limited to 0.24%, 0.16%, and 0.12% of the 3.5 mm, 4.5 mm, and 5.5 mm insulation for an applied voltage of 6 kV. At 12 kV, the region stretched a distance of 3.6%, 2.6%, and 0.96% of the 3.5 mm, 4.5 mm, and 5.5 mm insulation. Due to the significant localization of the high electric field values, experimental testing would be required to test if the insulation would breakdown under these applied voltages. It should be noted these maximum values are purely simulation and do not represent actual electric field values. Additionally, the sharp point in the electrode geometry likely contributed to the high electric values at this location. To increase accuracy of the results, a curvature should be considered to represent a more realistic electrode geometry in future evaluations. One limitation in the electric field simulation is that it does not include the electrical wires guided to and attached to the electrodes. The ground wire was in reality 1.5 mm closer to the high voltage electrode than the grounded shielding which may result in a potential breakdown to their first.

4. PLASMA STUDY AND LIMITATIONS

4.1 Model Overview

4.1.1 Purpose

Stable, repeatable plasma generation is necessary in a plasma medicine device. The precise control of the power input to the plasma (discharge power) is crucial in the selectively killing of cancer cells. The effect of different design and operating parameters on the plasma is unknown for this specific plasma device and must be investigated. The purpose of the plasma study was to evaluate the effect of various design and operating parameters on the plasma generation and power input to the plasma. Specifically, the electrode spacing and applied voltage was varied. Simulations were performed for an electrode spacing of 5 mm, 10 mm, and 15 mm at applied voltage amplitudes of 5 kV, 7 kV, and 10 kV, which represent a possible low, moderate, and high operating voltage. The electron density, electron temperature, discharge current, and capacitive power input to the plasma were compared between the varied simulations. Values obtained in the COMSOL simulation were input into a post-simulation plasma chemistry model to calculate the reactive oxygen species densities present in the afterglow plasma region (outside the device). Based on these results, the preferred electrode spacing was selected for the application of in vivo cancer treatment. Prior to performing the study, the characteristics of the plasma were evaluated as discussed in the Theory section.

4.1.2 Theory

The characteristics of the plasma were investigated prior to running simulations in order to determine if the plasma could be assumed quasi-neutral and modeled with a fluids approach. Quasi-neutrality of the plasma means the densities of electrons and ions are equal. The distance over which quasi-neutrality is considered a valid assumption depends on factors such as the density and temperature of the plasma. The Debye length, the distance over which quasi-neutrality may breakdown, was calculated using Eq. 4.1, where ε_o is the permittivity of free space (8.854 x 10^{-12}

F/m), k_b is the Boltzmann constant (1.381 x 10^{-23} J/K), T_e is the electron temperature (in K), e is the elementary charge (1.602 x 10^{-19} C), and n_e is the electron density (in m^{-3}) [36]. For a conservative estimate of the plasma in this study (n_e = 10^{15} m^{-3} and k_bT_e = 5 eV), the Debye length was determined to be 0.53 mm. The plasma was considered quasi-neutral because the Debye length was much smaller than the length of the plasma system under investigation.

$$\lambda_d = (\frac{\varepsilon_o k_b T_e}{e^2 n_e})^{1/2} \tag{4.1}$$

COMSOL Simulation

A fluids approach was used to simulate low-temperature plasma in COMSOL Multiphysics. The electron density and mean electron energy were calculated by solving a pair of drift-diffusion equations. Eq. 4.2 and Eq. 4.3 show the electron continuity and flux equation, where n_e is the electron density, $\mathbf{\Gamma_e}$ is the electron flux, R_e is the rate of electron generation/loss, μ_e is the electron mobility, $\mathbf{E}$ is the electric field, and D_e is the electron diffusion coefficient.

$$\frac{\partial n_e}{\partial t} + \nabla \cdot \mathbf{\Gamma_e} = R_e \tag{4.2}$$

$$\mathbf{\Gamma_e} = -n_e(\mu_e \cdot \mathbf{E}) - D_e \nabla n_e \tag{4.3}$$

The electron energy density was solved for using the energy continuity equation shown in Eq. 4.4, where n_ε is the electron energy density, $\mathbf{\Gamma_\varepsilon}$ is the electron energy flux, and R_ε is the rate of energy loss/gain from inelastic collisions.

$$\frac{\partial n_\varepsilon}{\partial t} + \nabla \cdot \mathbf{\Gamma_\varepsilon} + \mathbf{E} \cdot \mathbf{\Gamma_e} = R_\varepsilon \tag{4.4}$$

The energy rate from inelastic collisions was obtained from Eq. 4.5, where S_{en} is the collisional power loss, Q is an external heat source, Q_{gen} is a generalized heat source, and q is the electron

charge.

$$R_\varepsilon = S_{en} + \frac{Q + Q_{gen}}{q} \tag{4.5}$$

The electron energy flux equation is shown in Eq. 4.6, where μ_ε is the electron energy mobility and D_ε is the electron energy diffusion coefficient.

$$\mathbf{\Gamma_\varepsilon} = -n_\varepsilon(\mu_\varepsilon \cdot \mathbf{E}) - D_\varepsilon \nabla n_\varepsilon \tag{4.6}$$

The source coefficients, R_e and R_ε, were determined by the plasma chemistry using rate coefficients. The electron source term is presented by Eq. 4.7, where x_j is mole fraction of the target species for reaction j, k_j is the rate coefficient for reaction j, and N_n is the total number density.

$$R_e = \sum_{j=1}^{M} x_j k_j N_n n_e \tag{4.7}$$

The electron energy loss was acquired by summing the collisional energy loss over all reactions as expressed in Eq. 4.8, where where $\Delta\varepsilon_j$ is the energy loss from reaction j. The rate coefficients were obtained from cross-section data.

$$R_\varepsilon = \sum_{j=1}^{P} x_j k_j N_n n_e \Delta\varepsilon_j \tag{4.8}$$

The electron diffusivity, energy mobility, and energy diffusivity were computed using Einstein's relation for a Maxwellian EEDF as shown in Eq. 4.9.

$$D_e = \mu_e T_e,\ \mu_\varepsilon = \frac{5}{3}\mu_e,\ D_\varepsilon = \mu_e T_e \tag{4.9}$$

The mean electron energy (in eV), $\overline{\varepsilon}$, was determined from the electron density and electron energy density using Eq. 4.10. The electron temperature (in eV) is related to the mean electron energy as expressed in Eq. 4.11.

$$\overline{\varepsilon} = \frac{n_\varepsilon}{n_e} \tag{4.10}$$

$$T_e = \frac{2}{3}\overline{\varepsilon} \tag{4.11}$$

For non-electron species, the mass fraction of each species was computed using Eq. 4.12, where w_k is the mass fraction of the k_{th} species, ρ is the density of the mixture, **u** is the mass averaged fluid velocity vector, $\boldsymbol{j_k}$ is the diffusion flux vector, and R_k is the rate expression for species k.

$$\rho\frac{\partial w_k}{\partial t} + \rho(\mathbf{u}\cdot\nabla)w_k = \nabla\cdot\boldsymbol{j_k} + R_k \tag{4.12}$$

The electric field was calculated by solving Poisson's equation (Eq. 4.13) in the plasma region and Laplace's equation (Eq. 4.14) in the dielectric material, where ε_o is the permittivity of free space, ε_r is the relative permittivity, ρ_c is the space charge density, and *V* is the applied potential.

$$-\nabla\cdot\varepsilon_o\varepsilon_r\nabla V = \rho_c \tag{4.13}$$

$$-\nabla^2 V = 0 \tag{4.14}$$

$$\mathbf{E} = -\nabla V \tag{4.15}$$

The space charge density was automatically computed based on the plasma chemistry using the expression described in Eq. 4.16, where Z_k is charge number of species k and n_k is the number density of species k.

$$\rho_c = q(\sum_{k=1}^{N} Z_k n_k - n_e) \tag{4.16}$$

The system of equations were solved by a time-dependent solver in COMSOL.

Afterglow Chemistry Model

The rate equations were formulated based on the production and losses of each species and took the general form of Eq. 4.17, where [N] is the number density of species "N".

$$\frac{[\mathrm{N}]}{dt} = \sum \text{Production} - \sum \text{Loss} \tag{4.17}$$

The production and loss rates were formed from the reactants of each reaction. For a reaction of the general form aA + bB $\rightarrow$ cC + dD, the production rate for species C would be expressed as Eq. 4.18, where k is the rate coefficient for the reaction, [A] is the number density of species A, a is the coefficient of species A, [B] is the number density of species B, and b is the coefficient of species B. Using the same reaction, the loss rate for species A would be expressed as Eq. 4.19.

$$\text{Rate} = k[\mathrm{A}]^{\mathrm{a}}[\mathrm{B}]^{\mathrm{b}} \tag{4.18}$$

$$\text{Rate} = -k[\mathrm{A}]^{\mathrm{a}}[\mathrm{B}]^{\mathrm{b}} \tag{4.19}$$

4.1.3 Model Setup

COMSOL Simulation

The co-axial plasma device was investigated using a 1D plasma model. The device was simplified to a 1D domain representation as shown in Figure 4.1. The computational domain consists of two electrodes separated by dielectric barrier layers of 1.175 mm thickness. The gap between the two dielectric barriers (electrode spacing), X, was varied from 5 mm to 20 mm. A mesh consisting of 735, 1235, and 1735 elements, with refinement around the walls, was generated for electrode spacings of 5 mm, 10 mm, 15 mm, and 20 mm, respectively.

A sinusoidal voltage of the form shown in Eq. 4.20 was defined at the boundary of the high voltage electrode, where V_o is the voltage amplitude, t is time, and ω is the angular frequency equal to $2\pi f$. The frequency, f, was set to 20 kHz and the voltage amplitude was varied from 5 kV to 10

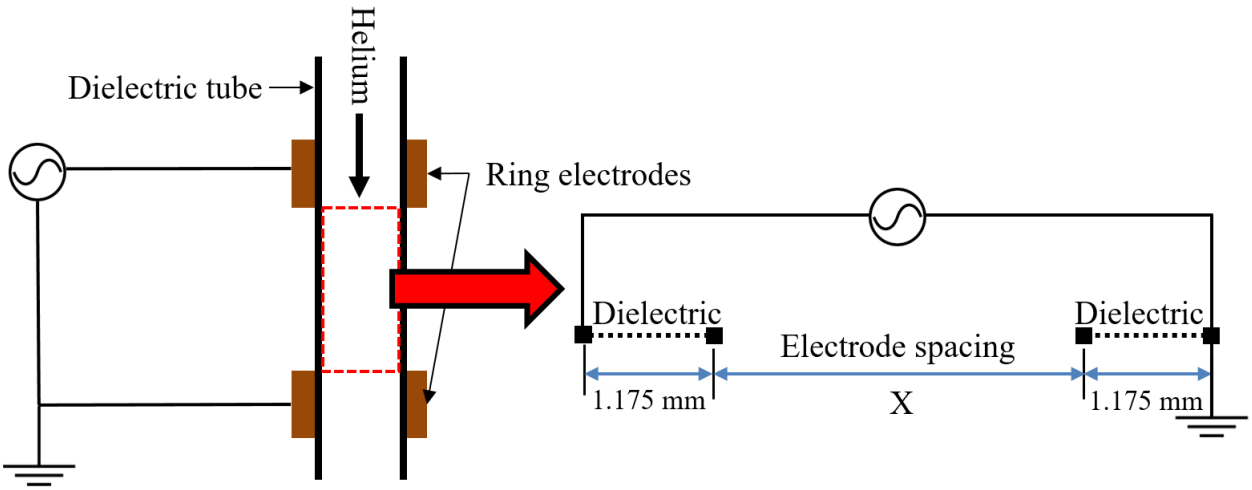

Figure 4.1: Co-axial plasma device converted to 1D computational domain (not to scale) for plasma simulation.

kV.

$$V = V_o sin(\omega t) \tag{4.20}$$

The boundary of the ground electrode was defined as grounded having a voltage represented by Eq. 4.21.

$$V = 0 \tag{4.21}$$

The relative permittivity of the dielectric material, borosilicate glass, was specified to be 4.6 based on the manufacturer's data sheet [34]. The surface charge accumulation on the dielectric surface due to the difference in fluxes between electrons and ions was taken into account using the boundary condition described by Eq. 4.22, where **n** is the normal vector pointed toward the surface, $\mathbf{D}_1$ and $\mathbf{D}_2$ are the electric displacement fields on both sides of the dielectric surface, and ρ_s is the net charge density accumulated on the dielectric surface. The surface charge density was automatically computed using Eq. 4.23, where $\boldsymbol{J_i}$ is total ion current density at the wall and $\boldsymbol{J_e}$ is the total electron current density at the wall.

$$\mathbf{n} \cdot (\mathbf{D}_1 - \mathbf{D}_2) = \rho_s \tag{4.22}$$

$$\frac{d\rho_s}{dt} = \mathbf{n} \cdot \boldsymbol{J_i} - \mathbf{n} \cdot \boldsymbol{J_e} \tag{4.23}$$

The loss of electrons to the walls and gain due to secondary emission effects were accounted for using the boundary condition for electron flux in Eq. 4.24 and electron energy flux in Eq. 4.25, where $v_{\text{e,th}}$ is the mean thermal velocity of an electron, γ_p is the secondary emission coefficient and ε_p is the mean energy of the secondary electrons. The mean electron thermal velocity was calculated from Eq. 4.26, where m_e is the electron mass.

$$\mathbf{n} \cdot \Gamma_e = (\frac{1}{2} v_{e,\text{th}} n_e) - \sum_p \gamma_p (\Gamma_p \cdot \mathbf{n}) \tag{4.24}$$

$$\mathbf{n} \cdot \Gamma_\varepsilon = (\frac{5}{6} v_{e,\text{th}} n_\varepsilon) - \sum_p \varepsilon_p \gamma_p (\Gamma_p \cdot \mathbf{n}) \tag{4.25}$$

$$v_{e,\text{th}} = \sqrt{\frac{8 k_b T_e}{\pi m_e}} \tag{4.26}$$

For secondary emission at the dielectric surfaces, the secondary electron coefficient was assumed to be equal to 0.01. This was consistent with the value used by [19].

Pure helium was assumed to fill the gap between the electrodes. Due to sufficient length between the grounded electrode and exit of the device, the reactions between helium and air were not considered. The plasma chemistry used in this model consisted of five species (e, He, He^+, He_2^+, He^*) and thirteen reactions. The helium reactions considered in this model are shown in Table 4.1 and are the same reactions used by [19]. The rate coefficients for the reactions were calculated by an offline Boltzmann solver, BOLSIG+, or adopted from the mentioned references. Figure 4.2 shows the rate coefficents for the reactions assuming a Maxwellian EEDF.

The gas temperature and pressure of the system was assumed to be constant at 300 K and 1 atm

Table 4.1: Helium reactions included in this study.

Index	Reaction	Rate coefficient	Energy (eV)	Remarks	Ref.
R1	$He + e \rightarrow He^* + e$	BOLSIG+	19.8	Excitation	[37]
R2	$He_2^+ + e \rightarrow He^* + He$	$5.386 \times 10^{-13}\ T_e^{-0.5}\ m^3\ s^{-1}$	–	Dissociative recomb.	[38]
R3	$He^* + e \rightarrow He + e$	$2.9 \times 10^{-15}\ m^3\ s^{-1}$	-19.8	De-excitation	[38]
R4	$He + e \rightarrow He^+ + 2e$	BOLSIG+	24.6	Ionization	[37]
R5	$He^* + e \rightarrow He^+ + 2e$	BOLSIG+	4.78	Ionization	[37]
R6	$2He^* \rightarrow He^+ + He + e$	$8.7 \times 10^{-16}\ m^3\ s^{-1}$	-15.0	Stepwise ionization	[39]
R7	$He^+ + 2He \rightarrow He_2^+ + He$	$1.1 \times 10^{-43}\ m^6\ s^{-1}$	–	Ion conversion	[39]
R8	$2He^* \rightarrow He_2^+ + e$	$2.03 \times 10^{-15}\ m^3\ s^{-1}$	–	Stepwise ionization	[39]
R9	$He_2^+ + e \rightarrow 2He$	$4.0 \times 10^{-15}\ m^3\ s^{-1}$	–	Dissociative recomb.	[40]
R10	$He^+ + e \rightarrow He^*$	$6.76 \times 10^{-19}\ T_e^{-0.5}\ m^3\ s^{-1}$	–	Two-body recomb.	[41]
R11	$He^+ + 2e \rightarrow e + He^*$	$6.186 \times 10^{-39}\ T_e^{-4.4}\ m^6\ s^{-1}$	–	Three-body recomb.	[42]
R12	$He^+ + He + e \rightarrow He^* + He$	$6.66 \times 10^{-42}\ T_e^{-2.0}\ m^6\ s^{-1}$	–	Three-body recomb.	[42]
R13	$He_2^+ + He + e \rightarrow He^* + 2He$	$3.5 \times 10^{-39}\ m^6\ s^{-1}$	–	Dissociative recomb.	[42]

Note:
Units: Electron temperature T_e (eV).

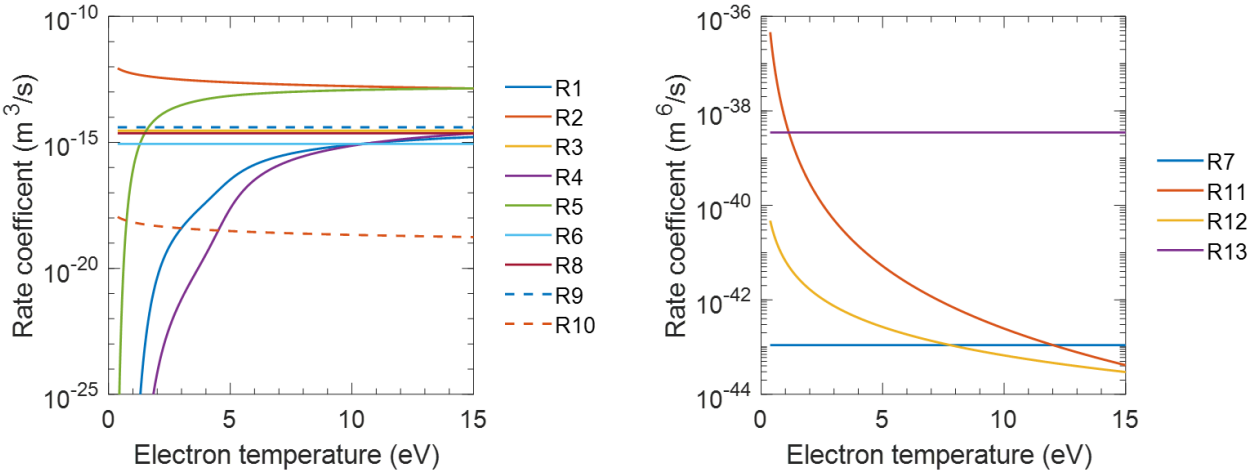

Figure 4.2: Rate coefficients of (a) two-body reactions and (b) three-body reactions assuming a Maxwellian EEDF.

for this work. A constant background electron and ion density of 10^7 cm^{-3} was assumed initially. The simulations were run with a time dependent solver in COMSOL for a duration of 50 voltage periods with time steps of 0.125 μs. The results were evaluated at the end of the duration to ensure a periodic steady state solution was reached.

Afterglow Chemistry Model

A 0D plasma chemistry model was created following the procedural flow shown in Figure 4.3 to investigate the concentration of reactive oxygen species in the afterglow region of plasma. Major production and loss channels of reactive oxygen species in the afterglow were identified based on the works of [21], [43], and [44]. The species presented in Table 4.2 were included in the model.

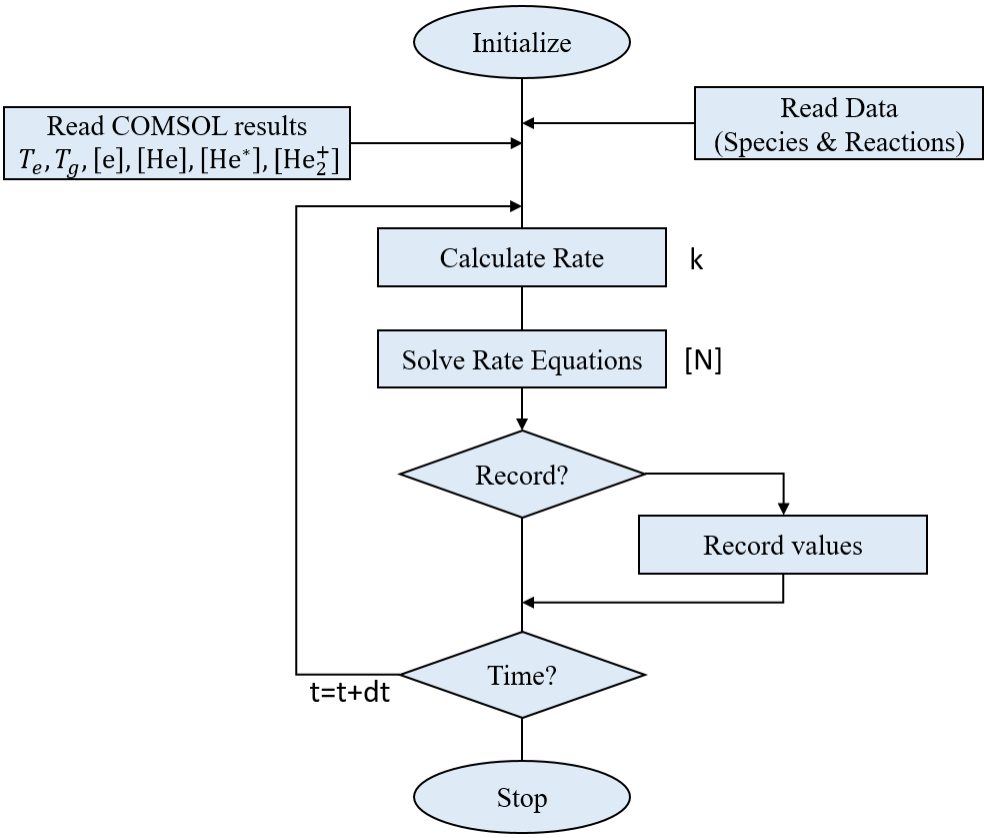

Figure 4.3: Flow chart describing the process of the afterglow chemistry model.

The reactions presented in Table B.1 were considered to play a prominent role in the generation and loss of reactive oxygen species present in the afterglow region of the plasma. These reactions were adopted from [21] and [43]. The dominant reactions, denoted by their labels in Table B.1, contributing to the total production/loss of each species are summarized in Table 4.3.

Table 4.2: Plasma species included in the afterglow chemistry model.

Neutral species	Feed Gas	He
	Impurities/Ambient air	N_2 (80%), O_2 (20%)
	Reactive species	He^*
		O, $O_2(^1D)$, O_3
		H, OH, HO_2, H_2O_2
Ions	Positive	He_2^+
		O_2^+
	Negative	O_2^-
Electron		e

Table 4.3: Dominant reactions of production and loss of species in the afterglow plasma region included in chemistry model.

Species	Production Reactions	Loss Reactions
O	A1, C8	C4, C5, C10
$O_2(^1D)$	C3, G1	A2, A3, C8
O_3	C10, C13	C2, C3, and C7
H	C4	C7, C11, C14
OH	C5, C7, C8	C4
HO_2	C11, C14	C5, C8, C9
H_2O_2	C12, C15	C6
O_2^+	B1, C1	D1, D2, E1, F1
O_2^-	A4, A5, A6	E1, F1, F2

Upon completion of the COMSOL simulations, the helium species number densities ([He], [He^*], [He_2^+]), electron density ([e]), and electron temperature (T_e) were spatially and temporally averaged over the last voltage cycle for each simulation. Additionally, the gas temperature (T_g), which was kept constant at 300 K throughout the simulations, was documented. The temperature values were input into the rate coefficient equations and solved. The resulting rate coefficients as well as the number densities from COMSOL were input into rate equations governing the production and loss of reactive oxygen species. N_2 was assumed to have a constant background number density of 1.96 x 10^{19} cm^{-3}. The flow rate of O_2 into the plasma was accounted for using Equation 4.27, where V_{O_2} is the inflow rate (in $cm^{-3}s^{-1}$), $[O_2]_b$ is the background number density of O_2 (4.89 x 10^{18} cm^{-3}), v_{diff} is the diffusion velocity, and d_{jet} is the diameter of the tube (4 mm).

$$V_{O_2} = [\mathrm{O_2}]_b \frac{v_{diff}}{d_{jet}} \tag{4.27}$$

The diffusion velocity of O_2 was determined to be 446 m/s using the equation (Eq. 4.28) for mean thermal speed, where T_g is the gas temperature (in K) and m_g is the mass of a single O_2 molecule (5.31 x 10^{26} kg).

$$v_{diff} = \sqrt{\frac{8k_bT_g}{\pi m_g}} \tag{4.28}$$

A system of 10 ODEs with 10 unknown species number densities were solved in MATLAB using ode45, which utilizes a fourth-order Runge-Kutta method. The model was run for a duration of 2.5 ms with time steps of 100 ns.

4.2 Results and Discussion

The plasma discharge characteristics, including electron density distribution, electron temperature distribution, discharge current, and discharge power, were evaluated for various electrode spacings and applied voltages. The results were examined after a periodic steady state solution was reached. To analyze the results to this 1D problem, the solution was extruded into two dimensions with the extra dimension being time.

The electron density distribution across various discharge gaps for an applied voltage of 5 kV is shown in Figure 4.4. The electron density was highest near the cathode and decreased across the discharge gap. The 5 mm gap yielded the highest electron density of 2.69 x 10^9 cm^{-3}. The 10 mm gap produced a slightly lower electron density, but the bulk of the concentration extended a further distance spatially per voltage cycle. The electrode density was significantly lower for a discharge gap of 15 mm with a maximum electron density 5.29 x 10^8 cm^{-3}. The 20 mm gap yielded a further reduced electron density. Overall, at an applied voltage of 5 kV, the plasma region containing the higher values of electron density was spatially localized near the cathode and spanned less than half of the discharge gap per voltage cycle in each of the gap sizes. Additionally, the electron density was particularly lower for the 15 mm and 20 mm electrode gaps and of the magnitude 10^8 cm^{-3}.

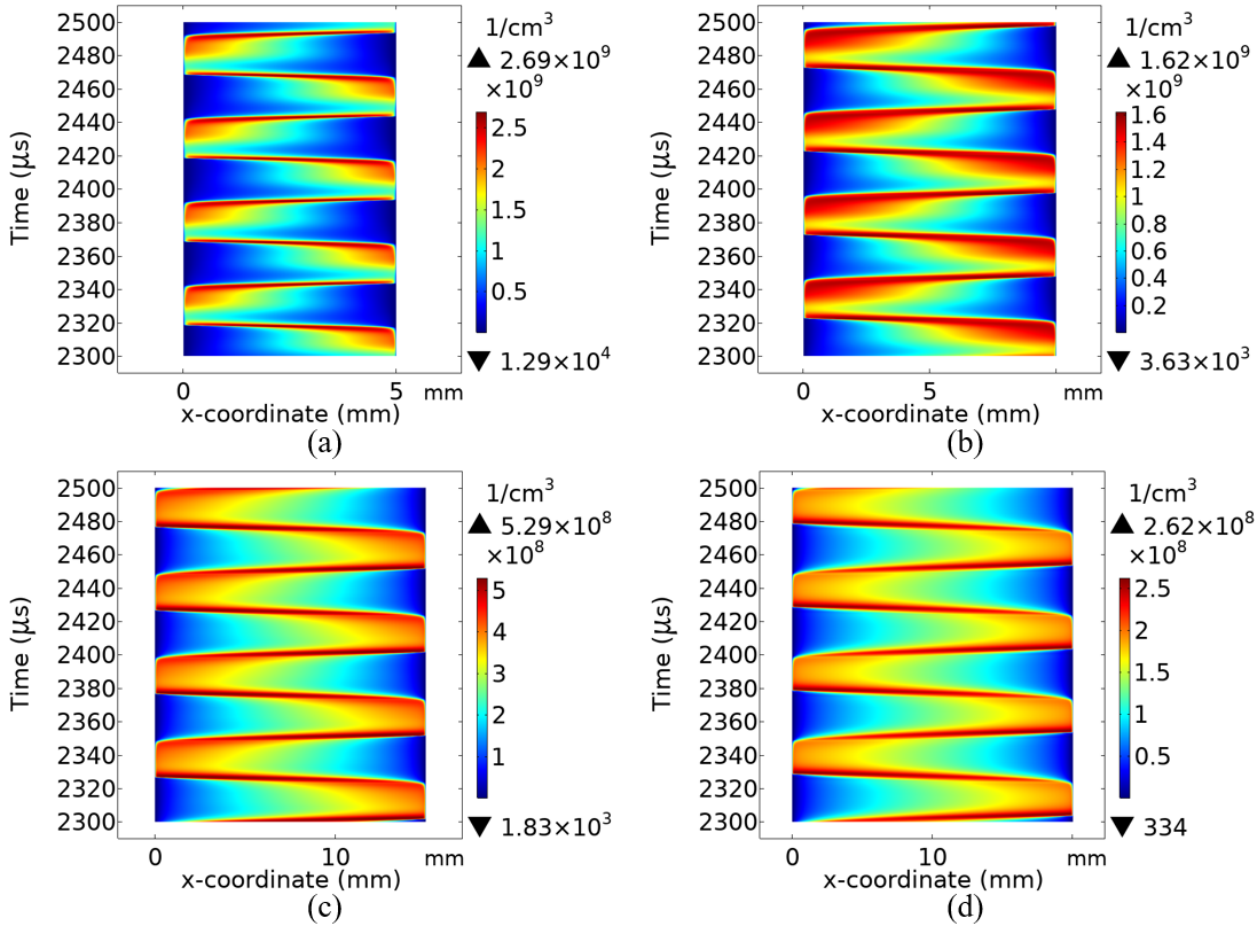

Figure 4.4: Surface plots showing electron density across various discharge gaps ((a) 5 mm gap, (b) 10 mm gap, (c) 15 mm gap, (d) 20 mm gap) for 4 voltage periods from an applied voltage of 5 kV.

The electron density across various discharge gaps for an applied voltage of 7 kV is shown in Figure 4.5. For a discharge gap of 5 mm, the maximum electron density was 4 x 10^9 cm^{-3}. The bulk of electron density, shown in red, expanded approximately a third of the 5 mm gap per voltage cycle. The electron density increased slightly for the 10 mm gap, and the bulk of the electron concentration was expanded over half of the discharge gap per voltage cycle. For the 15 mm gap, the maximum electron density was lower at 3.1 x 10^9 cm^{-3}, but the bulk of the electron density expanded approximately two-thirds of the 15 mm gap. The 20 mm gap yielded a lower maximum electron density of 1.03 x 10^9 cm^{-3} and the electron density remained relatively constant near the cathode over each voltage cycle. Overall, at the applied voltage of 7 kV, the bulk of the

electron concentration increased spatially with increasing discharge gaps up to 15 mm.

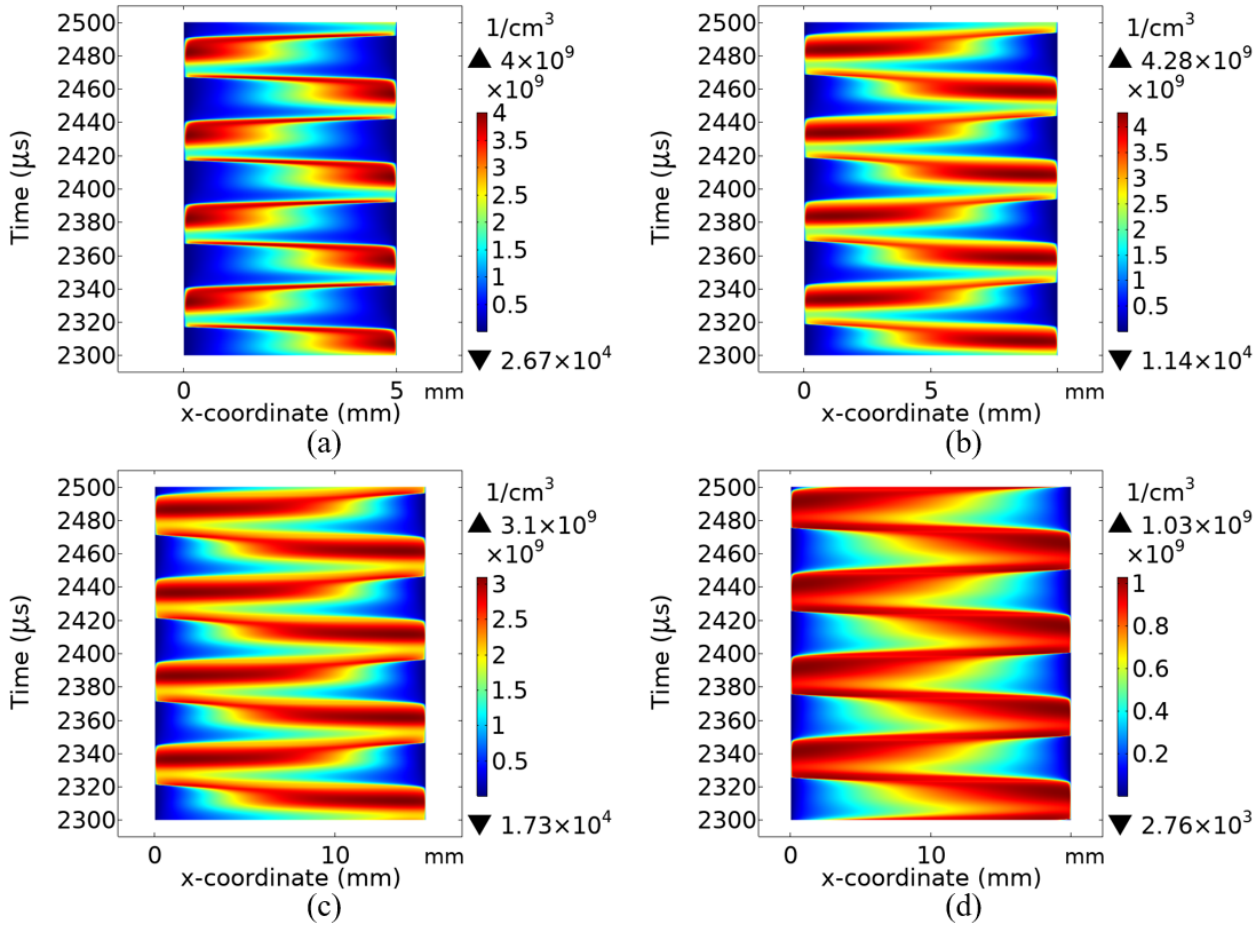

Figure 4.5: Surface plots showing electron density across various discharge gaps ((a) 5 mm gap, (b) 10 mm gap, (c) 15 mm gap, (d) 20 mm gap) for 4 voltage periods from an applied voltage of 7 kV.

The electron density across various discharge gaps for an applied voltage of 10 kV is shown in Figure 4.6. An applied voltage of 10 kV yielded the highest electron densities for each discharge gap. For a gap of 5 mm, the maximum electron density was 6.73 x 10^9 cm^{-3}, and the bulk electron concentration expanded a distance nearly half of the 5 mm gap. The 10 mm gap yielded the highest maximum electron density at 7.05 x 10^9 cm^{-3}, and the bulk electron concentration expanded a distance approximately two-thirds of the 10 mm gap. The 15 mm gap produced an electron density

with a slightly lower maximum electron density of 6.69 x 10^9 cm^{-3}, but the bulk of the concentration expanded a distance of approximately three-quarters of the 15 mm gap. The 20 mm gap yielded a marginally lower maximum electron density, but the bulk of the concentration extended a distance over three-quarters of the 20 mm gap. Overall, at an applied voltage of 10 kV, the bulk of the electron concentration was more defined and grew spatially with increasing discharge gap.

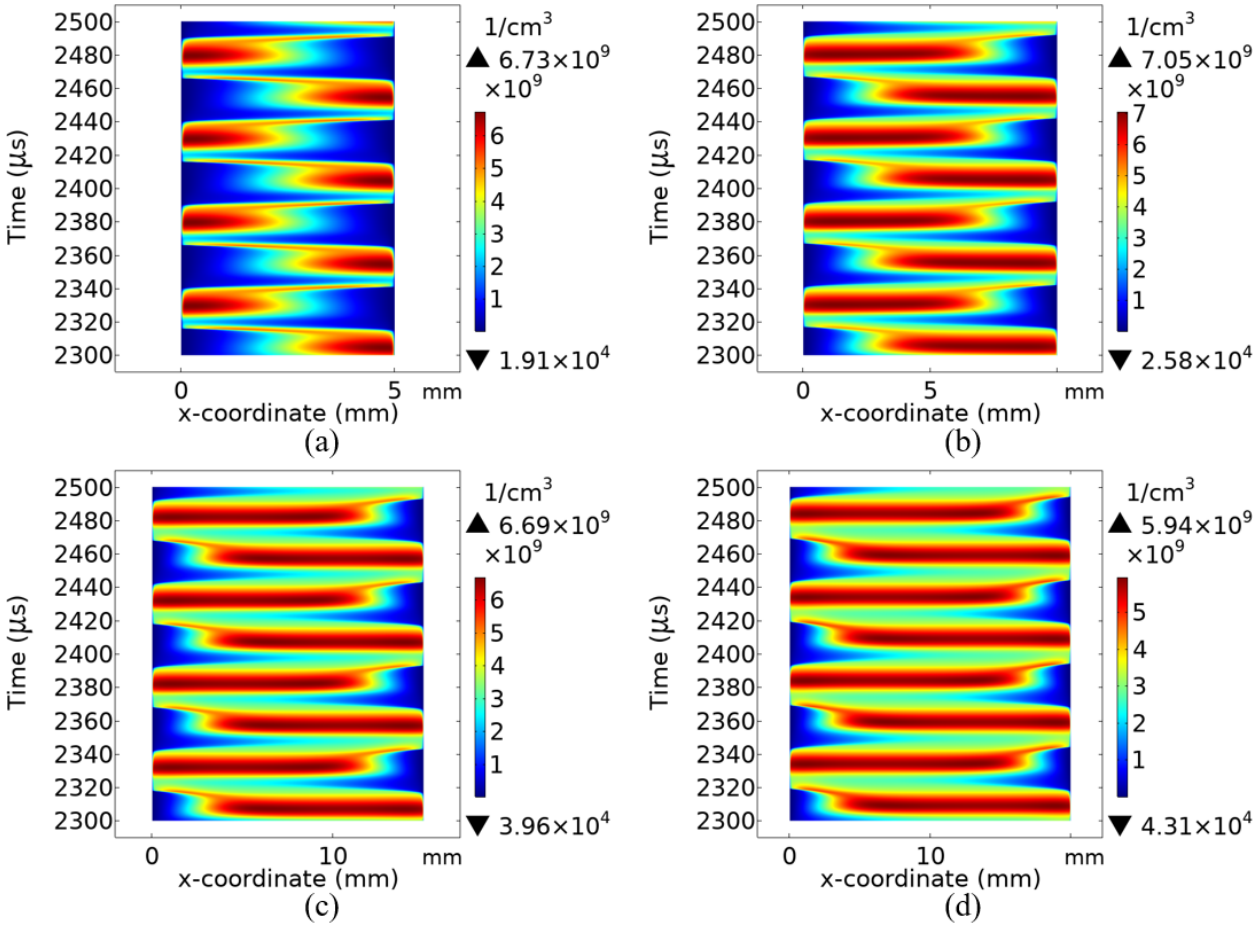

Figure 4.6: Surface plots showing electron density across various discharge gaps ((a) 5 mm gap, (b) 10 mm gap, (c) 15 mm gap, (d) 20 mm gap) for 4 voltage periods from an applied voltage of 10 kV.

The electron densities for the various applied voltages and discharge gaps were spatially and temporally averaged over a single voltage cycle. The variations of the average electron densities

with applied voltages and electrode spacings are presented in Figure 4.7. It should be noted the y-axis is log scale and the mentioned interpretations were drawn without this scale applied. As shown in Figure 4.7(a), the electron density increased linearly with the increasing applied voltage for electrode spacings of 5 mm, 10 mm, and 15 mm. For a gap of 20 mm, the electron density increased in an exponential manner. The maximum average electron density produced by a fixed applied voltage varied based on the electrode gap. As shown in Figure 4.7(b), the electron density decreased with the electrode gap for an applied voltage of 5 kV. For applied voltages of 7 kV and 10 kV, the density increased first and then decreased with the electrode gap. At applied voltages of 5 kV, 7 kV, and 10 kV the maximum average electron density was observed at electrode spacings of 5 mm, 10 mm, and 15 mm, respectively.

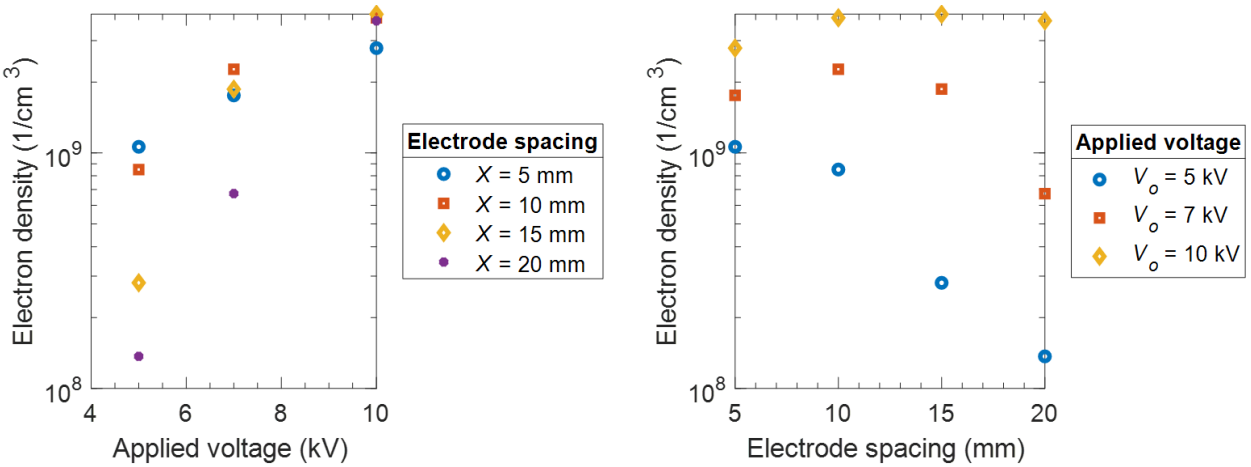

Figure 4.7: (a) Variation of the electron density with the applied voltage under different electrode gaps, (b) Variation of electron density with the electrode gap.

The electron temperature for the various applied voltages and discharge gaps were spatially and temporally averaged over a single voltage cycle. The variations of the average electron temperature with applied voltages and electrode spacings are presented in Figure 4.8. As shown in Figure 4.8(a), the electron temperature remained relatively constant at 4.5 eV with the increasing applied voltage for an electrode spacing of 5 mm. For a gap of 10 mm, the electron temperature decreased

slightly as applied voltage was increased. The 15 mm and 20 mm spacings experienced a transition at 7 kV from increasing temperature to decreasing temperature with voltage increase. The average maximum electron temperature produced by a fixed applied voltage did not vary based on the electrode gap as the maximum temperature was produced at a spacing of 5 mm for all voltages. As shown in Figure 4.8(b), the electron temperature decreased with the electrode gap for all applied voltages.

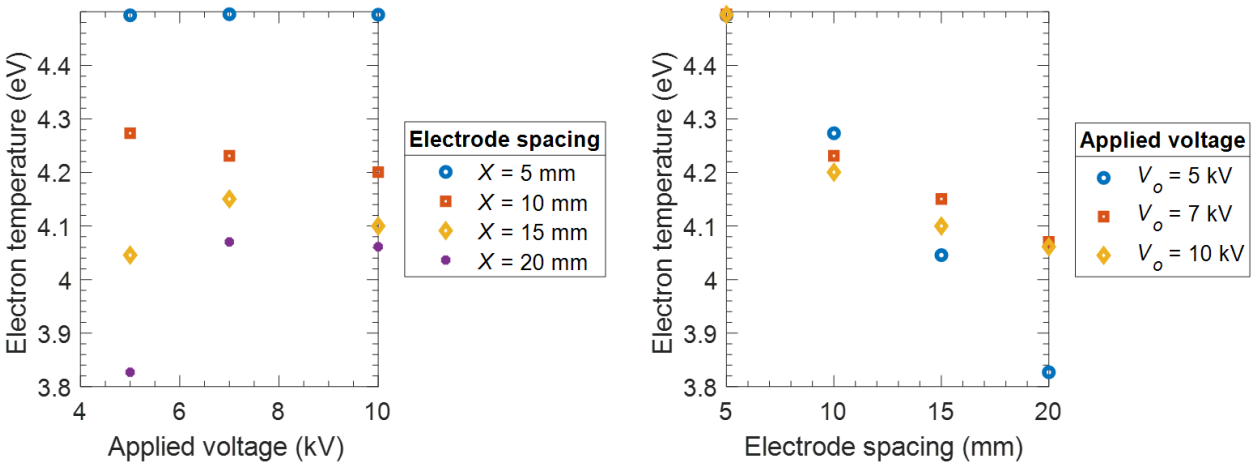

Figure 4.8: (a) Variation of the electron temperature with the applied voltage under different electrode gaps, (b) Variation of electron temperature with the electrode gap.

The applied voltage and discharge current waveforms generated over a single voltage period for various electrode spacings at applied voltages of 5 kV, 7 kV, and 10 kV are shown in Figure A.1, Figure A.2, and Figure A.3. These waveforms are representative of a capacitive discharge as the voltage lags the current. The variations of the peak discharge current with applied voltages and electrode spacings are presented in Figure 4.9. As shown in Figure 4.9(a), the discharge current increased linearly with the increasing applied voltage for electrode spacings of 5 mm, 10 mm, and 15 mm. For a gap of 20 mm, the current increased in an exponential manner. The maximum discharge current produced by a fixed applied voltage varied based on the electrode gap. As shown in Figure 4.9(b), the discharge current decreased with the electrode gap for applied voltages of 5

kV and 7 kV. For an applied voltage 10 kV, the current increased first and then decreased with the electrode gap. Thus, the electrode spacing determines the critical value upon which the current transitions from increasing to decreasing with a fixed applied voltage. This transition was not seen for applied voltages of 5 kV and 7 kV because electrode spacings less than 5 mm were not studied. At applied voltages of 5 kV, 7 kV, and 10 kV, the maximum discharge current was observed at electrode spacings of 5 mm, 5 mm and 10 mm, respectively.

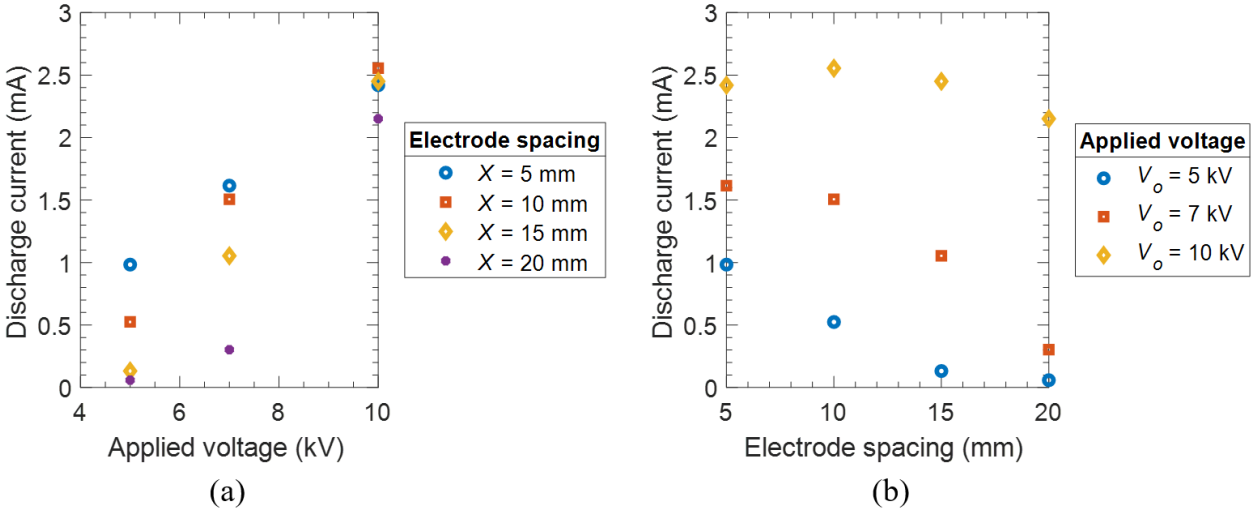

Figure 4.9: (a) Variation of the discharge current with the applied voltage under different electrode gaps, (b) Variation of discharge current with the electrode gap.

The instantaneous discharge power waveforms generated over a single voltage period for various electrode spacings at applied voltages of 5 kV, 7 kV, and 10 kV are shown in Figure A.4, Figure A.5, and A.6. The variations of average discharge power with applied voltages and electrode spacings are presented in Figure 4.10. As shown in Figure 4.10(a), the discharge power increased linearly with the increasing applied voltage for electrode spacings of 5 mm, 10 mm, and 15 mm. For an electrode spacing of 20 mm, the power increased exponentially with an increase in applied voltage. The maximum discharge power produced by a fixed applied voltage varied based on the electrode gap. As shown in Figure 4.10(b), the discharge power increased first and then decreased with the electrode gap for applied voltages of 5 kV and 7 kV. For an applied voltage

10 kV, the power increased with the electrode gap. Due to the short range of electrode spacings studied, a decrease was not observed at this voltage. At applied voltages of 5 kV, 7 kV, and 10 kV the maximum discharge power was observed at electrode spacings of 5 mm, 15 mm, and 20 mm, respectively.

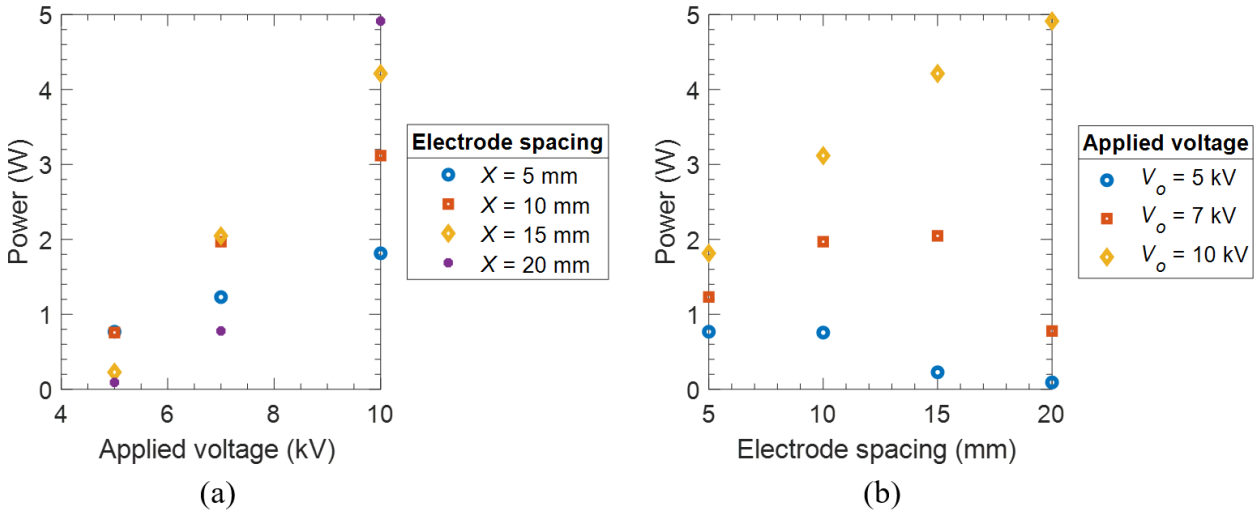

Figure 4.10: (a) Variation of the discharge power with the applied voltage under different electrode gaps, (b) Variation of discharge power with the electrode gap.

From the afterglow chemistry model, the number densities for reactive oxygen species were computed in the afterglow region of the plasma (outside the device) and evaluated at a time of 2.5 ms after exiting the tube, which would be at an estimated distance of 10 mm based on a helium flow velocity of 3.979 m/s. The plasma power generated from applied voltages of 5 kV, 7 kV, and 10 kV for various electrode spacings was plotted against the number density of the ROS produced under the resulting discharge. The ROS investigated include atomic oxygen (O), singlet-delta oxygen ($O_2(^1D)$), ozone (O_3), hydroxyl (OH), hydroperoxyl (HO_2), hydrogen peroxide (H_2O_2), and superoxide (O_2^-).

The number density of O in the afterglow region of the plasma produced using various electrode spacings is shown in Figure 4.11. Number density monotonically increased with increasing power. However, at a power of approximately 3 W the growth was halted. The concentration of O varied

from 3.1 x 10^{15} cm^{-3} to 1.2 x 10^{16} cm^{-3} for an electrode spacing of 5 mm. A 10 mm spacing produced a comparable profile with densities ranging from 1.9 x 10^{15} cm^{-3} to 1.6 x 10^{16} cm^{-3}. The number density dropped off a considerable amount at their lowest powers for 15 mm and 20 mm electrode spacings and did not yield concentrations exceeding those of 10 mm at their highest powers.

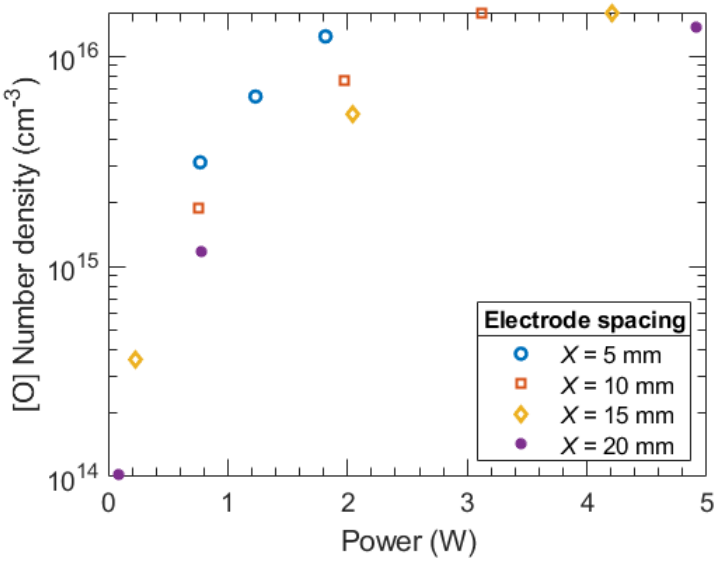

Figure 4.11: Number density of O in afterglow plasma region in relation to plasma power generated with various electrode spacings.

The number density of $O_2(^1D)$ in the afterglow region of the plasma produced using various electrode spacings is shown in Figure 4.12. Number density monotonically increased with increasing power, but the growth was stunted at a power over approximately 3 W. A 5 mm electrode spacing produced $O_2(^1D)$ concentrations ranging from 9.4 x 10^{18} cm^{-3} to 3 x 10^{19} while a 10 mm electrode spacing yielded similar results with an increase in concentration from 6.1 x 10^{18} cm^{-3} to 4.3 x 10^{18} cm^{-3}. Both 15 mm and 20 mm electrode spacings generated significantly lower $O_2(^1D)$ number densities at their lowest powers in comparison to the other electrode spacings and did not produce concentrations greater than the 10 mm spacing at higher powers.

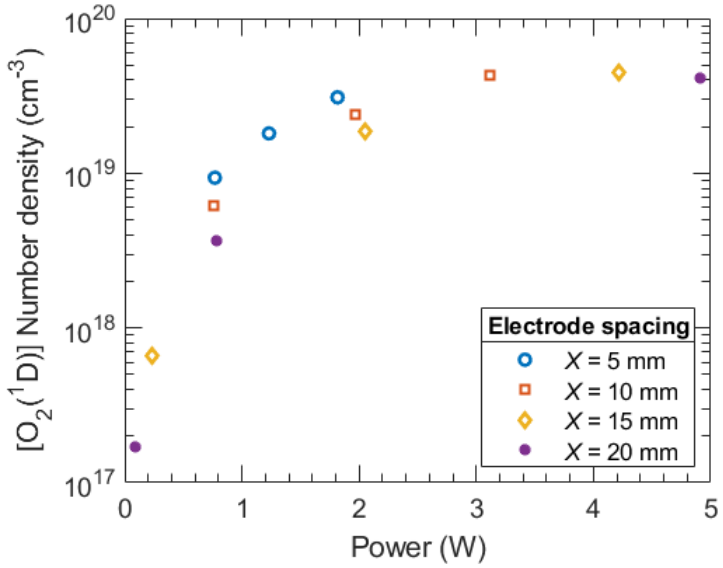

Figure 4.12: Number density of $O_2(^1D)$ in afterglow plasma region in relation to plasma power generated with various electrode spacings.

The number density of O_3 produced in the afterglow region of the plasma for various electrode spacings is shown in Figure 4.13. Number density monotonically decreased with increasing power for electrode spacings of 5 mm and 10 mm. However, the 15 mm and 20 mm spacings experienced a transition from increasing density to decreasing density with power increase, and therefore, a non-monotonic trend was observed. A 10 mm electrode spacing generated the highest concentrations of O_3 across the operating voltage range but all spacings produced densities of the magnitude 10^{18} cm^{-3}.

The number density of OH produced in the afterglow region of the plasma for various electrode spacings is shown in Figure 4.14. Number density monotonically increased with increasing power for electrode spacings of 5 mm and 10 mm. The 15 mm and 20 mm spacings experienced a transition from decreasing density to increasing density with power increase, and thus, a non-monotonic trend was seen. A 10 mm electrode spacing produced the highest concentration of OH at a power of 3.1 W. However, the variation in the OH number density was minimal for the different electrode spacings as they all fell within a span of 0.08 x 10^{12} cm^{-3}.

The number density of HO_2 produced in the afterglow region of the plasma for various elec-

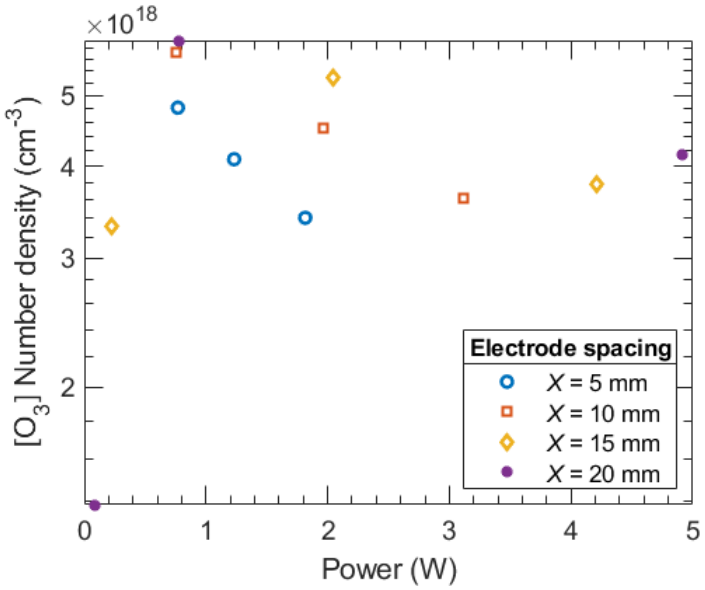

Figure 4.13: Number density of O_3 in afterglow plasma region in relation to plasma power generated with various electrode spacings.

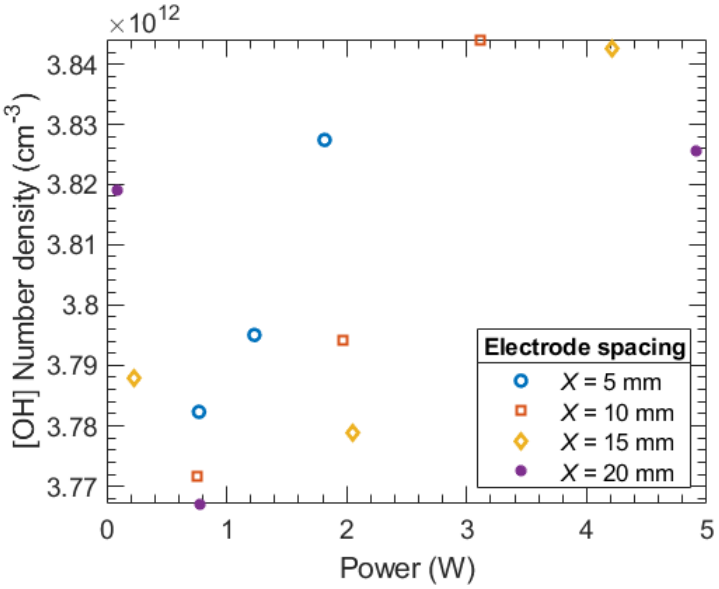

Figure 4.14: Number density of OH in afterglow plasma region in relation to plasma power generated with various electrode spacings.

trode spacings is shown in Figure 4.15. Number density monotonically increased with increasing power from about 2.0 x 10^9 cm^{-3} to 2.3 x 10^9 cm^{-3} for an electrode spacing of 5 mm. For a spacing

of 10 mm, the density remained relatively constant at 1.9 x 10^9 cm $^{-3}$ before increasing to 2.2 x 10^9 cm^{-3}. The 15 mm and 20 mm spacings experienced a transition from decreasing density to increasing density with power increase, and consequently, a non-monotonic trend was observed. This resulted in more variation in the HO_2 concentration in comparison to the other electrode spacings. All spacings produced densities of the magnitude 10^9 cm^{-3}.

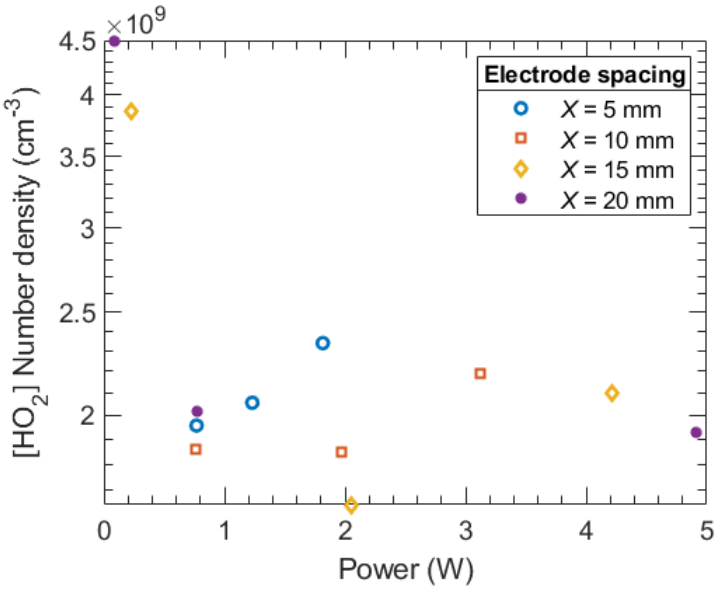

Figure 4.15: Number density of HO_2 in afterglow plasma region in relation to plasma power generated with various electrode spacings.

The number density of H_2O_2 produced in the afterglow region of the plasma for various electrode spacings is shown in Figure 4.16. Number density monotonically decreased with increasing power for electrode spacings of 5 mm and 10 mm. The 15 mm and 20 mm spacings experienced a transition from increasing density to decreasing density with power increase, and therefore, a non-monotonic trend was seen. However, the variation in the H_2O_2 number density was minimal for the different electrode spacings as they all fell within a span of 0.04 x 10^{12} cm^{-3}.

The density of the oxygen ions, O_2^+ and O_2^-, in the afterglow plasma region declined significantly on the time scale of a few μs. It was assumed that the afterglow plasma at 2.5 ms (10 mm

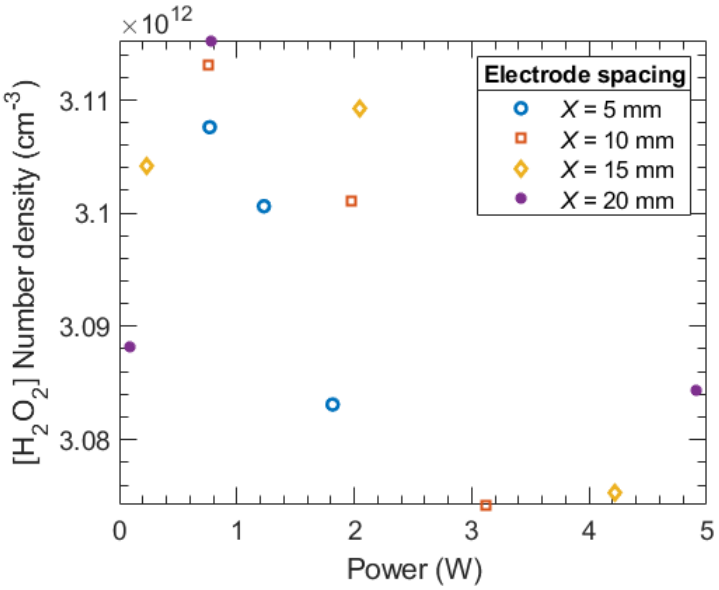

Figure 4.16: Number density of H_2O_2 in afterglow plasma region in relation to plasma power generated with various electrode spacings.

from exit of tube) would be essentially charge free. Thus, the analysis of O_2^- was excluded. This finding was consistent with that of [45].

Ultimately, the low plasma powers and the resulting discharge characteristics generated at the lower end of the operating voltage range prevented larger electrode spacings (15 mm and 20 mm) from producing consistently high concentrations of ROS across the investigated voltage range. Additionally, the higher powers they were able to produce from a high applied voltage did not produce ROS concentrations exceeding those from the 10 mm spacing. Both 5 mm and 10 mm electrode spacings were able to produce relatively high concentrations of ROS species across the operating voltage range. However, the 10 mm electrode spacing produced a slightly higher number densities at higher voltages. Therefore, a 10 mm electrode spacing would be considered the ideal electrode spacing in the application of cancer treatment as it has the potential to provide the highest concentrations of ROS in the afterglow plasma.

4.3 Limitations

There are several limitations in the state-of-the-art simulation technology that prohibits the thorough evaluation of plasma flow through a moving tip. The overwhelming reason is the time disparity between plasma and the movement of the tip. Plasma operates on a nanosecond time scale while the tip motion operates on a second time scale. Thus, a coupled, mulitiphysics approach is not feasible to study the plasma flow through a moving tip. Additionally, the solution to a computational problem must be resolved spatially by the mesh and temporally by the solver time step. This presents challenges in studying larger, multi-dimensional computational domains over an extended amount of time as these problems can be quite computationally expensive. Lastly, the physics involved in the modeling of plasma is complex. Consequentially, these limitations and difficulties required simplifications and assumptions to be made in the studying of this plasma device.

5. CONCLUSIONS

The feasiblity of a robotic plasma medicine device designed for in vivo use has been explored in terms of safety of efficacy. Due to the limitations in simulation technology, individual studies were performed to study the physics involved in the operation of a robotic plasma device including a neutral gas flow study, electrostatics study, and plasma study.

The characteristics of the gas flow indicated that the average velocity and flow rate would remain the same at the inlet and exit of the tube. This demonstrated that a prescribed inlet dosage would remain constant throughout the delivery process. The neutral gas flow study revealed the effect a dynamic tip has on the radial velocity profile exiting the device. Consequentially, this has the potential to increase the loss of charged species to the walls of the device as well as influence the even delivery of plasma products to a cancer cite. Thus, a decreased angular tip velocity would be required to reduce these potential effects when treating larger areas.

The electrostatics study showed that the electric field decayed through the insulation and was reduced to zero at the grounded shield. This ensured that there was no electric field outside of the device and would prevent any potential breakdown from occurring externally. Additionally, the region of the insulation containing electric field values greater than the insulation's dielectric strength was significantly localized. Therefore, it could not be determined if the insulation would breakdown under applied voltages of 6 kV and 12 kV and experimental testing would be required.

The plasma study demonstrated the effects of varying the electrode spacing and applied voltage on the discharge characteristics including electron density, electron temperature, discharge current, and plasma power. The 5 mm electrode spacing demonstrated the ability to produce a consistent plasma discharge with the least variance over the operating voltage range in comparison to the other electrode gaps. The 10 mm spacing yielded similar results but with increased values for electron density, discharge current, and power at higher voltages. The 15 mm and 20 mm electrode spacings yielded significantly lower values for electron density, electron temperature, discharge current, and power at a voltage of 5 kV but generated higher powers in comparison to the other electrode gaps

at a voltage of 10 kV. The afterglow chemistry model allowed a connection to made in terms of how the plasma discharge characteristics produced in the variance of applied voltage and electrode spacing effect a device's potential ability to treat cancer through the generation of reactive oxygen species including O, $O_2(^1D)$, O_3, OH, HO_2, H_2O_2, and O_2^-. Both 5 mm and 10 mm electrode spacings demonstrated the ability to produce relatively high concentrations of ROS species across the operating voltage range. However, the 10 mm electrode spacing produced slightly higher number densities at higher voltages and would be considered the ideal electrode spacing in the application of cancer treatment as it has the potential to provide the highest concentrations of ROS in the afterglow plasma.

In the future, a 2D plasma model with a 10 mm electrode spacing will be created to study the plasma flow into air. Specifically, the reactive oxygen and nitrogen species present at different operating distances will be investigated. Additionally, experimental testing will be required to validate the results.

REFERENCES

[1] A. M. Hirst, F. M. Frame, N. J. Maitland, and D. O'Connell, "Low temperature plasma: a novel focal therapy for localized prostate cancer?," *BioMed research international*, vol. 2014, 2014.

[2] B. McKinney, W. McKinney, S. Pattanshetti, and S. C. Ryu, "Feasibility study of in vivo robotic plasma medicine devices," in *2019 International Symposium on Medical Robotics (ISMR)*, pp. 1–7, IEEE, 2019.

[3] M. Laroussi, "Plasma medicine: a brief introduction," *Plasma*, vol. 1, no. 1, pp. 47–60, 2018.

[4] M. Keidar, "Plasma for cancer treatment," *Plasma Sources Science and Technology*, vol. 24, no. 3, p. 033001, 2015.

[5] N. Georgescu and A. R. Lupu, "Tumoral and normal cells treatment with high-voltage pulsed cold atmospheric plasma jets," *IEEE Transactions on Plasma Science*, vol. 38, no. 8, pp. 1949–1955, 2010.

[6] M. Vandamme, E. Robert, S. Pesnel, E. Barbosa, S. Dozias, J. Sobilo, S. Lerondel, A. Le Pape, and J.-M. Pouvesle, "Antitumor effect of plasma treatment on u87 glioma xenografts: preliminary results," *Plasma processes and polymers*, vol. 7, no. 3-4, pp. 264–273, 2010.

[7] J. L. Zirnheld, S. N. Zucker, T. M. DiSanto, R. Berezney, and K. Etemadi, "Nonthermal plasma needle: development and targeting of melanoma cells," *IEEE Transactions on Plasma Science*, vol. 38, no. 4, pp. 948–952, 2010.

[8] M. Keidar, R. Walk, A. Shashurin, P. Srinivasan, A. Sandler, S. Dasgupta, R. Ravi, R. Guerrero-Preston, and B. Trink, "Cold plasma selectivity and the possibility of a paradigm shift in cancer therapy," *British journal of cancer*, vol. 105, no. 9, p. 1295, 2011.

[9] L. Brullé, M. Vandamme, D. Riès, E. Martel, E. Robert, S. Lerondel, V. Trichet, S. Richard, J.-M. Pouvesle, and A. Le Pape, "Effects of a non thermal plasma treatment alone or in combination with gemcitabine in a mia paca2-luc orthotopic pancreatic carcinoma model," *PloS one*, vol. 7, no. 12, p. e52653, 2012.

[10] S. Mohades, N. Barekzi, and M. Laroussi, "Efficacy of low temperature plasma against scaber cancer cells," *Plasma Processes and Polymers*, vol. 11, no. 12, pp. 1150–1155, 2014.

[11] S. Mirpour, S. Piroozmand, N. Soleimani, N. J. Faharani, H. Ghomi, H. F. Eskandari, A. M. Sharifi, S. Mirpour, M. Eftekhari, and M. Nikkhah, "Utilizing the micron sized non-thermal atmospheric pressure plasma inside the animal body for the tumor treatment application," *Scientific reports*, vol. 6, p. 29048, 2016.

[12] S. Mohades, "Low temperature plasma for the treatment of epithelial cancer cells," 2017.

[13] E. Gjika, S. Pal-Ghosh, A. Tang, M. Kirschner, G. Tadvalkar, J. Canady, M. A. Stepp, and M. Keidar, "Adaptation of operational parameters of cold atmospheric plasma for in vitro treatment of cancer cells," *ACS applied materials & interfaces*, vol. 10, no. 11, pp. 9269–9279, 2018.

[14] G. Fridman, A. Shereshevsky, M. M. Jost, A. D. Brooks, A. Fridman, A. Gutsol, V. Vasilets, and G. Friedman, "Floating electrode dielectric barrier discharge plasma in air promoting apoptotic behavior in melanoma skin cancer cell lines," *Plasma Chemistry and Plasma Processing*, vol. 27, no. 2, pp. 163–176, 2007.

[15] M. Thiyagarajan, L. Waldbeser, and A. Whitmill, "Thp-1 leukemia cancer treatment using a portable plasma device.," *Studies in health technology and informatics*, vol. 173, pp. 515–517, 2012.

[16] S. Elmore, "Apoptosis: a review of programmed cell death," *Toxicologic pathology*, vol. 35, no. 4, pp. 495–516, 2007.

[17] A. M. Hirst, F. M. Frame, M. Arya, N. J. Maitland, and D. OâĂŹConnell, "Low temperature plasmas as emerging cancer therapeutics: the state of play and thoughts for the future," *Tumor Biology*, vol. 37, no. 6, pp. 7021–7031, 2016.

[18] M. Keidar, "A prospectus on innovations in the plasma treatment of cancer," *Physics of Plasmas*, vol. 25, no. 8, p. 083504, 2018.

[19] H. Haixin, H. Feng, Z. Ping, and J. Ouyang, "Numerical study of the influence of dielectric tube on propagation of atmospheric pressure plasma jet based on coplanar dielectric barrier discharge," *Plasma Science and Technology*, vol. 20, no. 5, p. 054010, 2018.

[20] W. Yan and D. J. Economou, "Gas flow rate dependence of the discharge characteristics of a helium atmospheric pressure plasma jet interacting with a substrate," *Journal of Physics D: Applied Physics*, vol. 50, no. 41, p. 415205, 2017.

[21] M. Hasan, *Numerical modelling of atmospheric pressure plasma jet discharges*. PhD thesis, University of Liverpool, 2016.

[22] S. Gadkari and S. Gu, "Numerical investigation of co-axial dbd: Influence of relative permittivity of the dielectric barrier, applied voltage amplitude, and frequency," *Physics of Plasmas*, vol. 24, no. 5, p. 053517, 2017.

[23] G. Gao, L. Dong, K. Peng, W. Wei, C. Li, and G. Wu, "Comparison of the surface dielectric barrier discharge characteristics under different electrode gaps," *Physics of Plasmas*, vol. 24, no. 1, p. 013510, 2017.

[24] B. Chen, Z. Tan, and X. Song, "Effects of the operating conditions on the electrical characteristics of pulse discharges in atmospheric-pressure pure helium," *IEEE Transactions on Plasma Science*, vol. 40, no. 4, pp. 1103–1109, 2012.

[25] D. Gidon, B. Curtis, J. A. Paulson, D. B. Graves, and A. Mesbah, "Model-based feedback control of a khz-excited atmospheric pressure plasma jet," *IEEE Transactions on Radiation and Plasma Medical Sciences*, vol. 2, no. 2, pp. 129–137, 2018.

[26] Y. Lyu, L. Lin, E. Gjika, T. Lee, and M. Keidar, "Mathematical modeling and control for cancer treatment with cold atmospheric plasma jet," *Journal of Physics D: Applied Physics*, vol. 52, no. 18, p. 185202, 2019.

[27] "(FEM) modeling: Comsol multiphysics and elmer," (accessed March 16, 2019). http://nanophysics.pl/comsol.php.

[28] "The finite element method (FEM)," (accessed March 16, 2019). https://www.comsol.com/multiphysics/finite-element-method.

[29] M. Rovitto, "Finite element method procedure in COMSOL multiphysics," (accessed March 16, 2019). http://www.iue.tuwien.ac.at/phd/rovitto/node72.html.

[30] J. Schäfer, R. Foest, A. Quade, A. Ohl, and K. Weltmann, "Local deposition of siox plasma polymer films by a miniaturized atmospheric pressure plasma jet (appj)," *Journal of Physics D: Applied Physics*, vol. 41, no. 19, p. 194010, 2008.

[31] S. Van Vrekhem, R. Morent, and N. De Geyter, "Deposition of a pmma coating with an atmospheric pressure plasma jet," *Journal of Coatings Technology and Research*, vol. 15, no. 4, pp. 679–690, 2018.

[32] A. Dubuc, P. Monsarrat, F. Virard, N. Merbahi, J.-P. Sarrette, S. Laurencin-Dalicieux, and S. Cousty, "Use of cold-atmospheric plasma in oncology: a concise systematic review," *Therapeutic advances in medical oncology*, vol. 10, p. 1758835918786475, 2018.

[33] J. E. Shigley, *Shigley's mechanical engineering design*. Tata McGraw-Hill Education, 2011.

[34] "Material properties: Glass code 7740," PYREX. (accessed November 15, 2018). http://glassfab.com/wp-content/uploads/2015/08/Corning-Pyrex.pdf.

[35] "Technical data sheet: Translucent epoxy, encapsulating potting compound (832c)," *MG Chemicals*. (accessed November 15, 2018). https://www.mgchemicals.com/downloads/tds/tds-832c-2parts.pdf.

[36] M. A. Lieberman, A. J. Lichtenberg, *et al.*, *Principles of plasma discharges and materials processing*, vol. 2. Wiley Online Library, 2005.

[37] G. Hagelaar and L. Pitchford, "Solving the boltzmann equation to obtain electron transport coefficients and rate coefficients for fluid models," *Plasma Sources Science and Technology*, vol. 14, no. 4, p. 722, 2005.

[38] Y. Wang and D. Wang, "Influence of impurities on the uniform atmospheric-pressure discharge in helium," *Physics of plasmas*, vol. 12, no. 2, p. 023503, 2005.

[39] Y. Sakiyama, D. B. Graves, J. Jarrige, and M. Laroussi, "Finite element analysis of ring-shaped emission profile in plasma bullet," *Applied Physics Letters*, vol. 96, no. 4, p. 041501, 2010.

[40] J. Pouvesle, A. Bouchoule, and J. Stevefelt, "Modeling of the charge transfer afterglow excited by intense electrical discharges in high pressure helium nitrogen mixtures," *The Journal of Chemical Physics*, vol. 77, no. 2, pp. 817–825, 1982.

[41] D. Breden, K. Miki, and L. Raja, "Self-consistent two-dimensional modeling of cold atmospheric-pressure plasma jets/bullets," *Plasma Sources Science and Technology*, vol. 21, no. 3, p. 034011, 2012.

[42] D.-X. Liu, P. Bruggeman, F. Iza, M.-Z. Rong, and M. G. Kong, "Global model of low-temperature atmospheric-pressure he+ h2o plasmas," *Plasma Sources Science and Technology*, vol. 19, no. 2, p. 025018, 2010.

[43] W. Van Gaens and A. Bogaerts, "Reaction pathways of biomedically active species in an ar plasma jet," *Plasma Sources Science and Technology*, vol. 23, no. 3, p. 035015, 2014.

[44] T. Murakami, K. Niemi, T. Gans, D. O'Connell, and W. G. Graham, "Chemical kinetics and reactive species in atmospheric pressure helium–oxygen plasmas with humid-air impurities," *Plasma Sources Science and Technology*, vol. 22, no. 1, p. 015003, 2012.

[45] T. Murakami, K. Niemi, T. Gans, D. O'Connell, and W. G. Graham, "Afterglow chemistry of atmospheric-pressure helium–oxygen plasmas with humid air impurity," *Plasma Sources Science and Technology*, vol. 23, no. 2, p. 025005, 2014.

[46] J. T. Gudmundsson and E. Thorsteinsson, "Oxygen discharges diluted with argon: dissociation processes," *Plasma Sources Science and Technology*, vol. 16, no. 2, p. 399, 2007.

[47] P. Cosby, "Electron-impact dissociation of oxygen," *The Journal of chemical physics*, vol. 98, no. 12, pp. 9560–9569, 1993.

[48] T. Jaffke, M. Meinke, R. Hashemi, L. G. Christophorou, and E. Illenberger, "Dissociative electron attachment to singlet oxygen," *Chemical physics letters*, vol. 193, no. 1-3, pp. 62–68, 1992.

[49] D. S. Stafford and M. J. Kushner, "O 2 (δ 1) production in he/ o 2 mixtures in flowing low pressure plasmas," *Journal of applied physics*, vol. 96, no. 5, pp. 2451–2465, 2004.

[50] Y. Itikawa, A. Ichimura, K. Onda, K. Sakimoto, K. Takayanagi, Y. Hatano, M. Hayashi, H. Nishimura, and S. Tsurubuchi, "Cross sections for collisions of electrons and photons with oxygen molecules," *Journal of Physical and Chemical Reference Data*, vol. 18, no. 1, pp. 23–42, 1989.

[51] H. Shimamori and R. W. Fessenden, "Thermal electron attachment to oxygen and van der waals molecules containing oxygen," *The Journal of Chemical Physics*, vol. 74, no. 1, pp. 453–466, 1981.

[52] R. Cardoso, T. Belmonte, G. Henrion, and N. Sadeghi, "Influence of trace oxygen on he (2 3s) density in a he–o2 microwave discharge at atmospheric pressure: behaviour of the time afterglow," *Journal of Physics D: Applied Physics*, vol. 39, no. 19, p. 4178, 2006.

[53] K. Niemi, J. Waskoenig, N. Sadeghi, T. Gans, and D. O'Connell, "The role of helium metastable states in radio-frequency helium-oxygen atmospheric pressure plasma jets: Measurement and numerical simulation," in *APS Meeting Abstracts*, 2011.

[54] J. Pouvesle, A. Khacef, J. Stevefelt, H. Jahani, V. Gylys, and C. B. Collins, "Study of two-body and three-body channels for the reaction of metastable helium atoms with selected atomic and molecular species," *The Journal of chemical physics*, vol. 88, no. 5, pp. 3061–3071, 1988.

[55] S. A. Smirnov, V. V. Rybkin, I. Kholodkov, and V. A. Titov, "Simulation of the processes of formation and dissociation of neutral particles in air plasma: kinetics of neutral components," *High temperature*, vol. 40, no. 3, pp. 323–330, 2002.

[56] W. B. DeMore, J. Margitan, M. Molina, R. Watson, D. Golden, R. Hampson, M. Kurylo, C. Howard, and A. Ravishankara, "Tables of rate constants extracted from chemical kinetics and photochemical data for use in stratospheric modeling. evaluation number 7," *International journal of chemical kinetics*, vol. 17, no. 10, pp. 1135–1151, 1985.

[57] Y. Sakiyama, D. B. Graves, H.-W. Chang, T. Shimizu, and G. E. Morfill, "Plasma chemistry model of surface microdischarge in humid air and dynamics of reactive neutral species," *Journal of Physics D: Applied Physics*, vol. 45, no. 42, p. 425201, 2012.

[58] F. J. Gordillo-Vázquez, "Air plasma kinetics under the influence of sprites," *Journal of Physics D: Applied Physics*, vol. 41, no. 23, p. 234016, 2008.

[59] O. Eichwald, M. Yousfi, A. Hennad, and M. D. Benabdessadok, "Coupling of chemical kinetics, gas dynamics, and charged particle kinetics models for the analysis of no reduction from flue gases," *Journal of applied physics*, vol. 82, no. 10, pp. 4781–4794, 1997.

[60] J. Manion, R. Huie, R. Levin, D. Burgess, V. Orkin, W. Tsang, W. McGivern, J. Hudgens, V. Knyazev, D. Atkinson, *et al.*, "Nist chemical kinetics database, standard reference database 17, version 7.0 (web version, release 1.6. 8, data version 2013.03); national institute of standards and technology, gaithersburg, md," *kinetics. nist. gov*.

[61] A. A. Konnov, "Implementation of the ncn pathway of prompt-no formation in the detailed reaction mechanism," *Combustion and Flame*, vol. 156, no. 11, pp. 2093–2105, 2009.

[62] M. H. Bortner and T. Baurer, "Defense nuclear agency reaction rate handbook," tech. rep., General Electric Co Philadelphia Pa Space Div, 1972.

[63] I. Kossyi, A. Y. Kostinsky, A. Matveyev, and V. Silakov, "Kinetic scheme of the non-equilibrium discharge in nitrogen-oxygen mixtures," *Plasma Sources Science and Technology*, vol. 1, no. 3, p. 207, 1992.

APPENDIX A

VOLTAGE, CURRENT, AND POWER WAVEFORMS

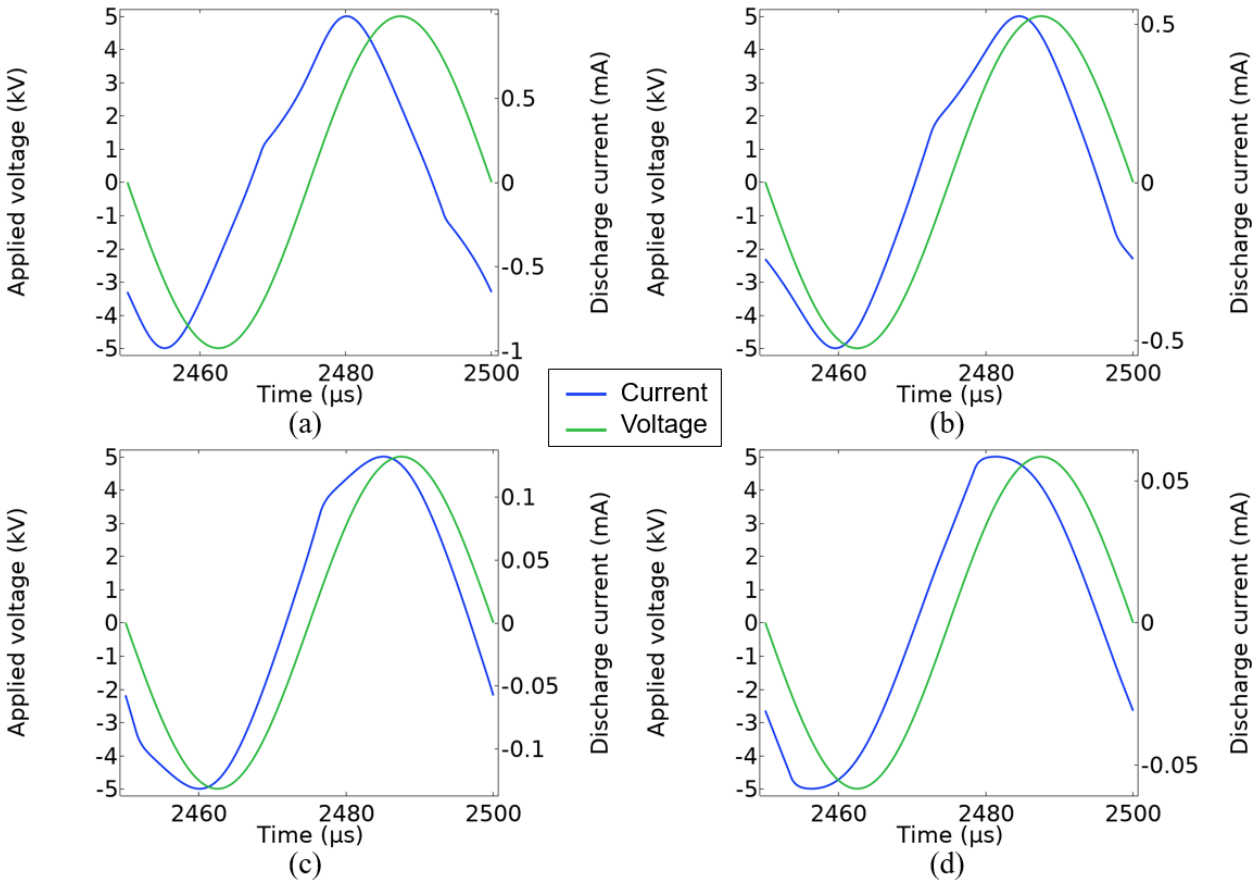

Figure A.1: Current and voltage waveforms over 1 voltage period for various electrode spacings ((a) 5 mm, (b) 10 mm, (c) 15 mm, (d) 20 mm) from an applied voltage of 5 kV.

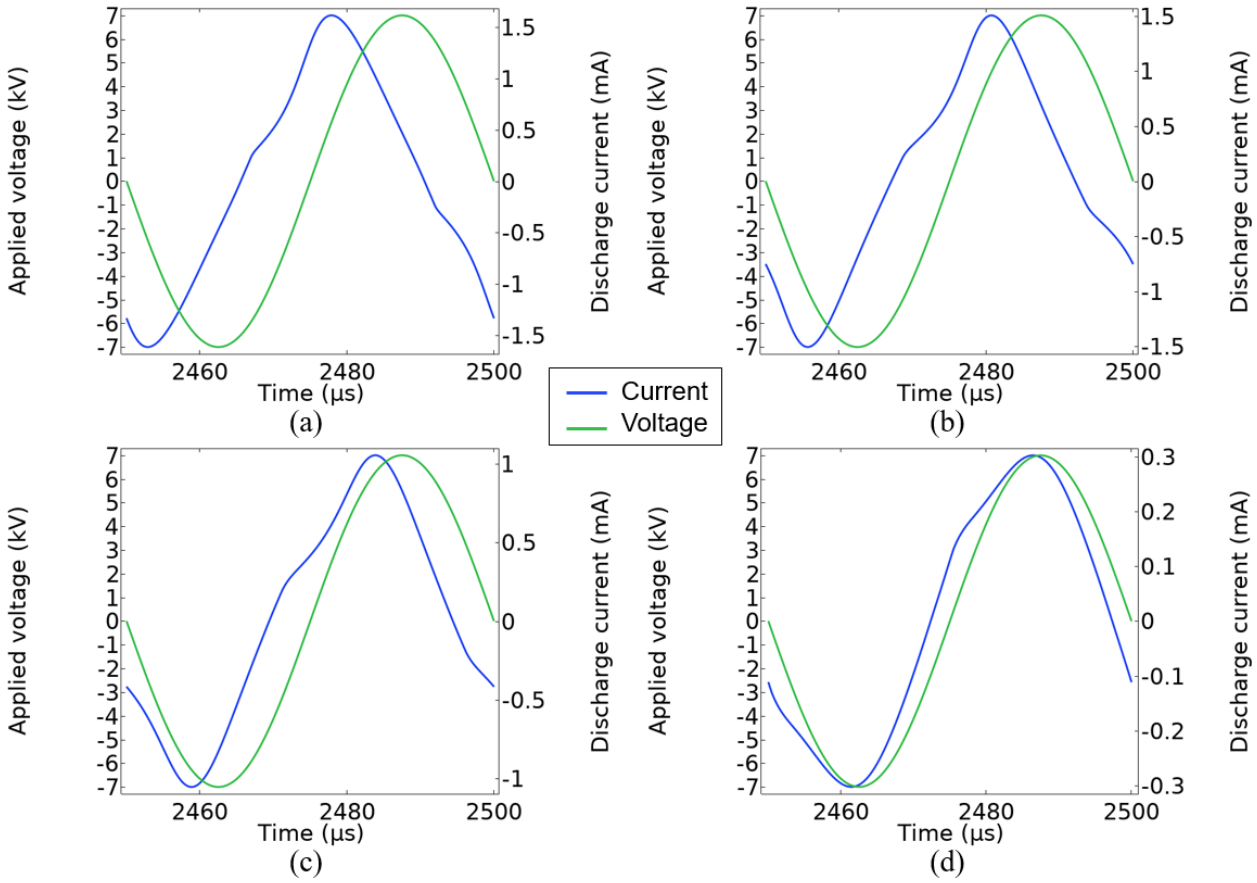

Figure A.2: Current and voltage waveforms over 1 voltage period for various electrode spacings ((a) 5 mm, (b) 10 mm, (c) 15 mm, (d) 20 mm) from an applied voltage of 7 kV.

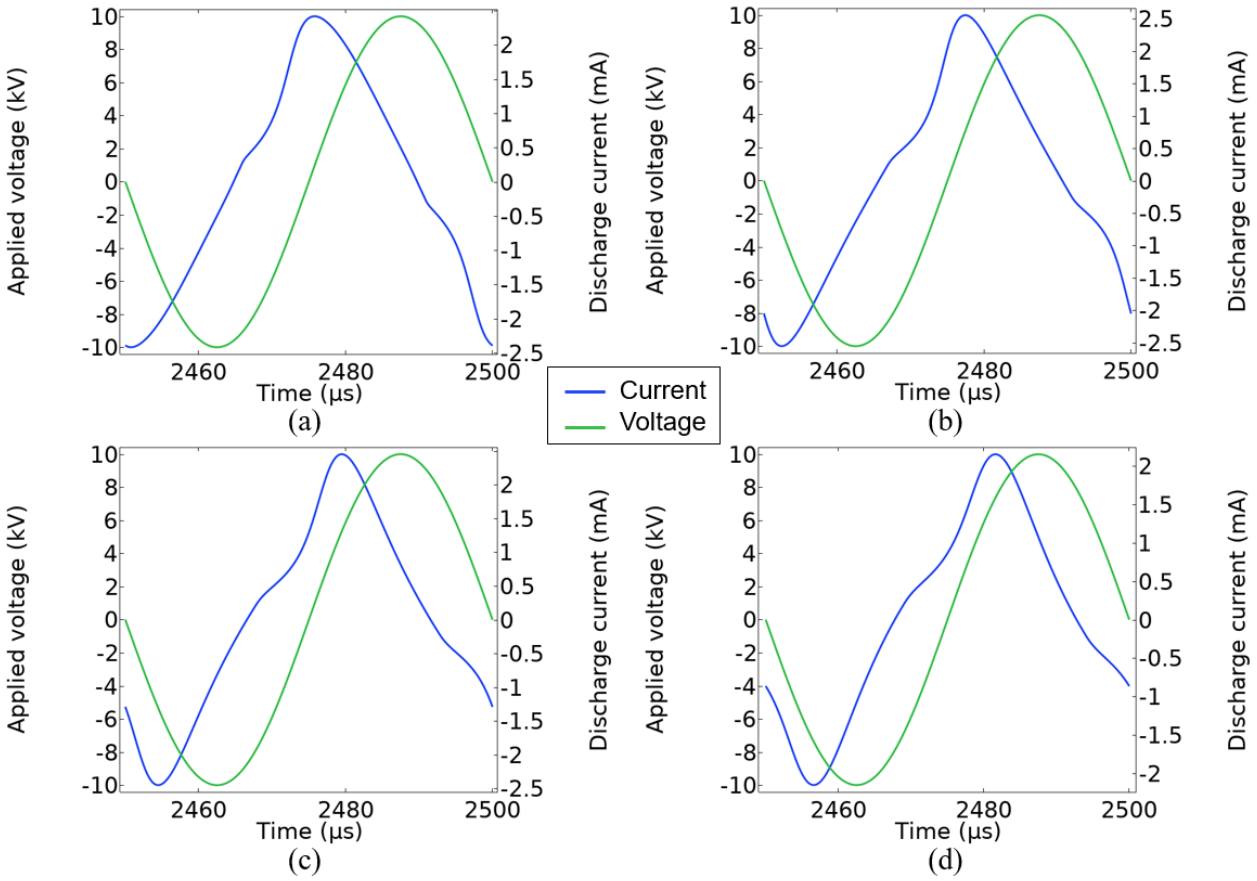

Figure A.3: Current and voltage waveforms over 1 voltage period for various electrode spacings ((a) 5 mm, (b) 10 mm, (c) 15 mm, (d) 20 mm) from an applied voltage of 10 kV.

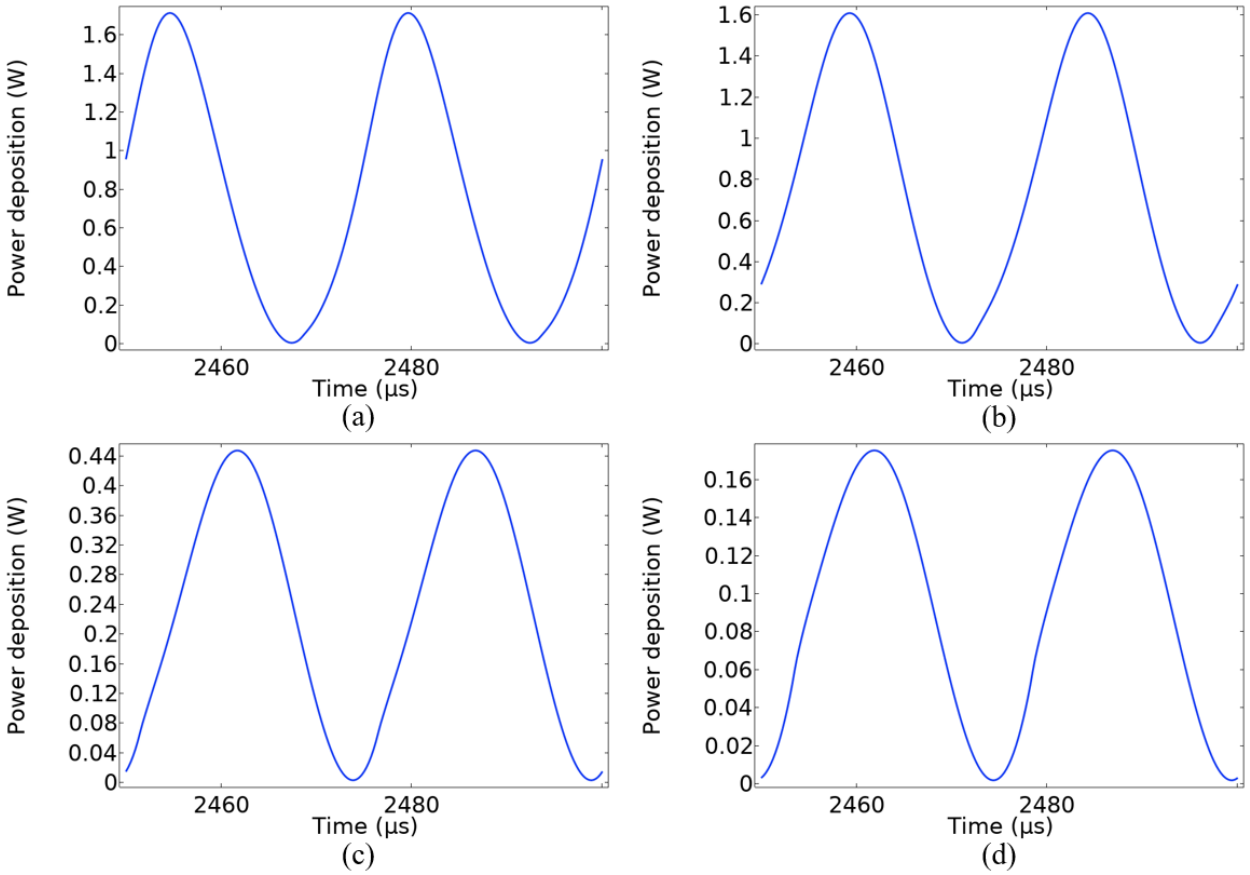

Figure A.4: Instantaneous power waveform over 1 voltage period for various electrode spacings ((a) 5 mm, (b) 10 mm, (c) 15 mm, (d) 20 mm) from an applied voltage of 5 kV.

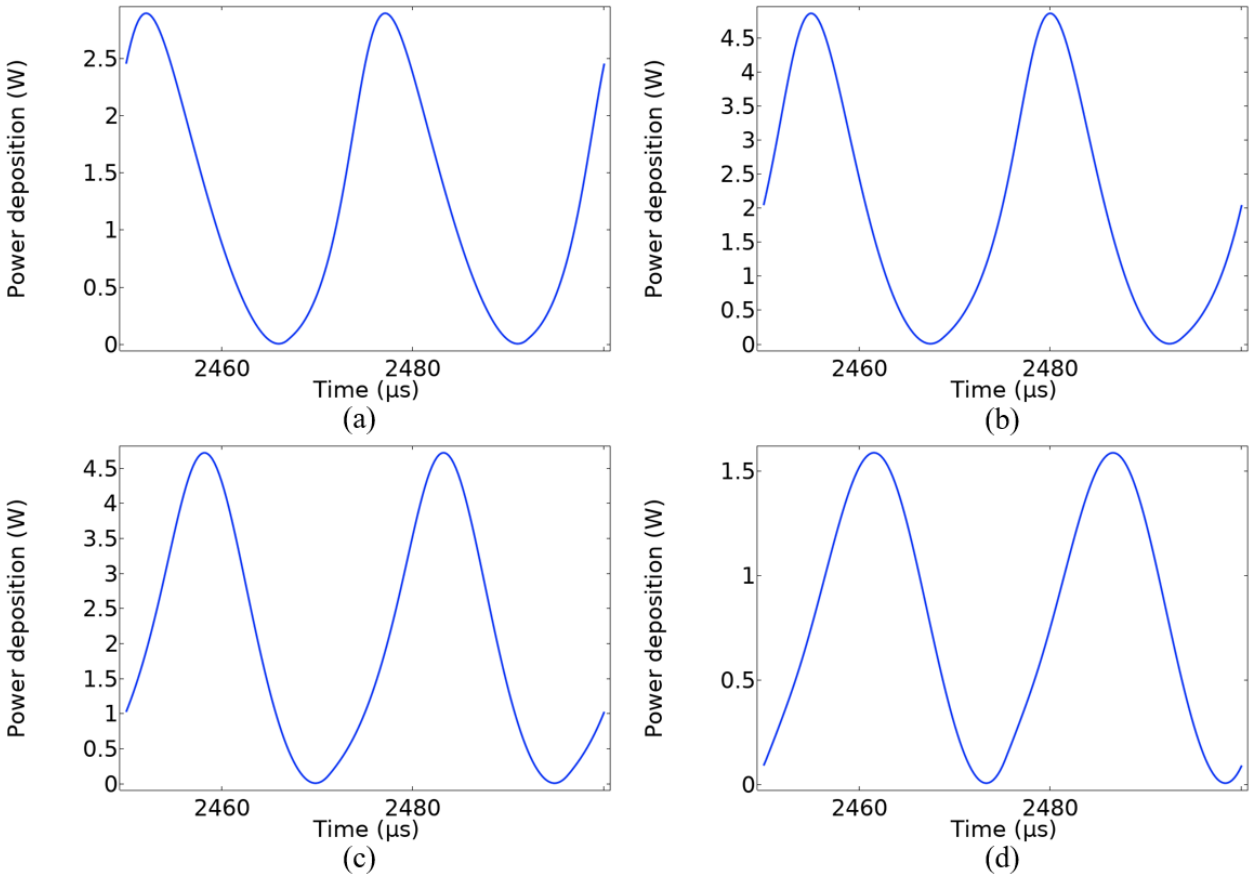

Figure A.5: Instantaneous power waveform over 1 voltage period for various electrode spacings ((a) 5 mm, (b) 10 mm, (c) 15 mm, (d) 20 mm) from an applied voltage of 7 kV.

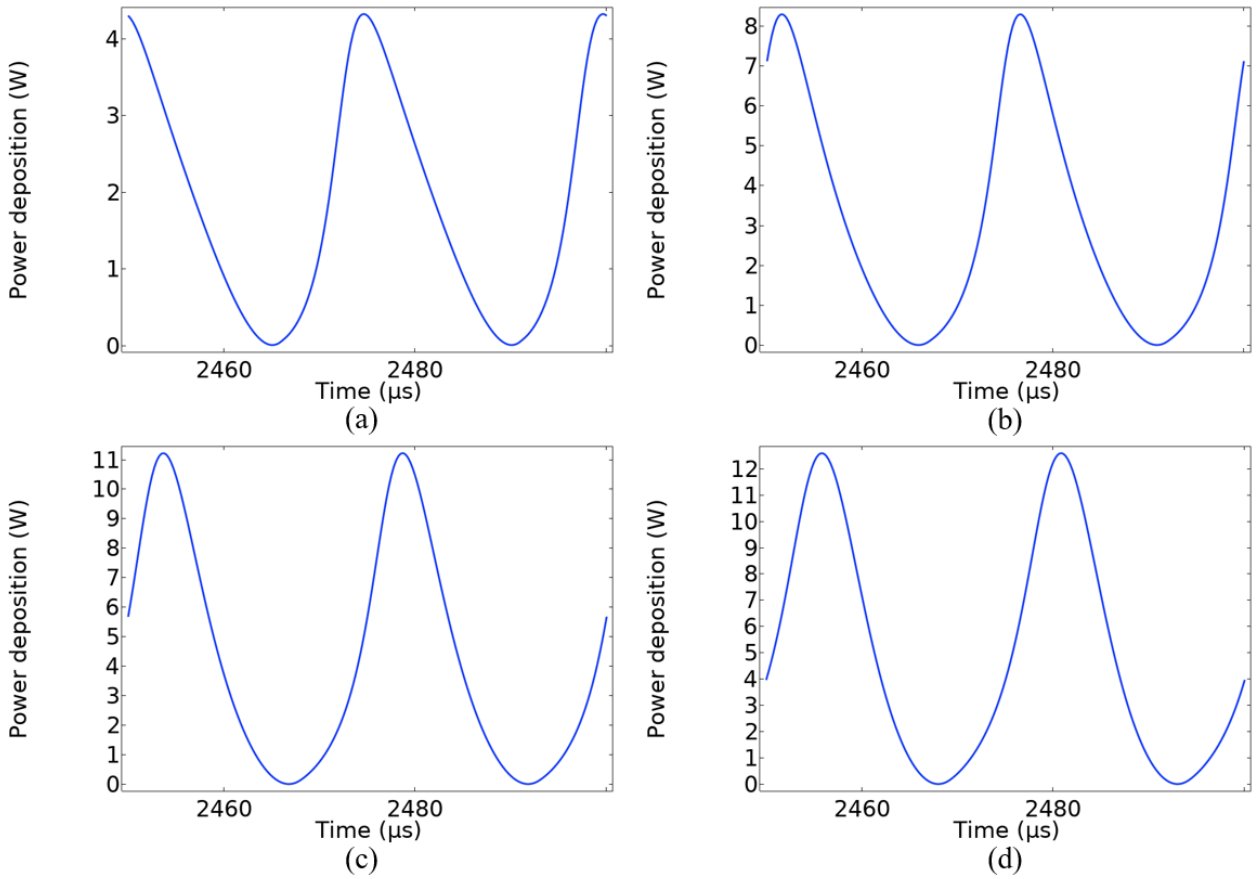

Figure A.6: Instantaneous power waveform over 1 voltage period for various electrode spacings ((a) 5 mm, (b) 10 mm, (c) 15 mm, (d) 20 mm) from an applied voltage of 10 kV.

APPENDIX B

AFTERGLOW PLASMA REACTIONS

Table B.1: Plasma reactions included in the afterglow chemistry model.

Index	Reaction	Rate coefficient	Ref.
	Electron/negative-ion reaction		
A1	e + O_2 → 2O + e	1.41 x 10^{-9} ${T_e}^{0.22}$ exp(-12.62/T_e)	[46, 47]
A2	e + $O_2(^1D)$ → 2O + e	1.41 x 10^{-9} ${T_e}^{0.22}$exp(-11.64/T_e)	[46, 48]
A3	e + $O_2(^1D)$ → O_2 + e	2.06 x 10^{-9} exp(-1.163/T_e)	[46]
A4	e + He + O_2 → He + O_2^-	3.6 x 10^{-31} ${T_e}^{-0.5}$	[49, 50]
A5	e + $2O_2$ → O_2 + O_2^-	3.6 x 10^{-31} ${T_e}^{-0.5}$	[49]
A6	e + O_2 + N_2 → N_2 + O_2^-	1.24 x 10^{-31} ${T_e}^{-0.5}$	[51]
	Positive-ion reaction		
B1	He_2^+ + O_2 → 2He + O_2^+	1.0 x 10^{-9} (T_g/300)$^{0.5}$	[42, 52]
	Neutral-species reaction		
C1	He^* + O_2 → He + O_2^+ + e	2.6 x 10^{-10}	[53, 54]
C2	O + O_3 → $2O_2$	8.00 x 10^{-12} exp(-2060/T_g)	[49]
C3	O + O_3 → O_2 + $O_2(^1D)$	6.49 x 10^{-13}	[55]
C4	O + OH → O_2 + H	2.2 x 10^{-11} exp(120/T_g)	[56]
C5	O + HO_2 → O_2 + OH	8.3 x 10^{-11} exp(-500/T_g)	[57]
C6	O + H_2O_2 → OH + HO_2	1.79 x 10^{-13} (T_g/300)$^{2.92}$ exp(-1394.0/T_g)	[42, 58]
C7	O_3 + H → O_2 + OH	7.78 x 10^{-11} (T_g/300)$^{0.2251}$exp(-327.8/T_g)	[58]
C8	$O_2(^1D)$ + HO_2 → O + O_2 + OH	1.66 x 10^{-11}	[59]
C9	H + HO_2 → 2OH	2.35 x 10^{-10} exp(-373.7/T_g)	[58]
C10	He + O + O_2 → He + O_3	3.4 x 10^{-34} (T_g/300)$^{-1.2}$	[49, 60]
C11	He + O_2 + H → He + HO_2	6.09 x 10^{-32} (T_g/300)$^{-0.80}$	[60]
C12	He + 2OH → He + H_2O_2	8.00 x 10^{-31} (T_g/300)$^{-0.80}$	[61]
C13	O + O_2 + N_2 → O_3 + N_2	1.1 x 10^{-34} exp(510/T_g)	[62]
C14	O_2 + N_2 + H → N_2 + HO_2	6.09 x 10^{-32} (T_g/300)$^{-0.80}$	[61]
C15	N_2 + 2OH → N_2 + H_2O_2	8.00 x 10^{-31} (T_g/300)$^{-0.90}$	[61]
	Positive-ion electron recomb.		
D1	O_2^+ + e → 2O	2.1 x 10^{-7} (T_e/T_g)$^{-0.63}$	[62]
D2	O_2^+ + 2e → O_2 +e	7.0 x 10^{-20} (T_e/T_g)$^{-4.5}$	[62]
	Two-body positive-ion negative-ion recomb.		
E1	O_2^+ + O_2^- → $2O_2$	4.2 x 10^{-7} (T_g/300)$^{-0.5}$	[62]
	Three-body/cluster-ion recomb.		
F1	O_2^+ + O_2^- + He → He + $2O_2$	2.0 x 10^{-25} (T_g/300)$^{-2.5}$	[42, 63]
F2	O_2^+ + O_2^- + N_2 → $2O_2$ + N_2	2.0 x 10^{-25} (T_g/300)$^{-2.5}$	[63]
	Electron-impact metastable production		
G1	e + O_2 → $O_2(^1D)$ + e	1.37 x 10^{-9} exp(-2.14/T_e)	[46, 48]

Note:
Units: Two-body reaction rate coefficient (cm^3 s^{-1}). Three-body reaction rate coefficient (cm^6 s^{-1}). Electron temperature T_e (eV). Gas (heavy particle) temperature T_g (K). Ratio of electron temperature to gas temperature (in D1,D2) T_e(K)/T_g(K) = T_e(eV)/T_g(eV).